Applied Mathematical Modelling 113 (2023) 475–513

Contents lists available at ScienceDirect

Applied Mathematical Modelling

journal homepage: www.elsevier.com/locate/apm

Hybrid absorbing scheme based on hyperelliptical layers with non-reflecting boundary conditions in scalar wave equations

Ruben Andres Salas[a], Andre Luis Ferreira da Silva[a], Luis Fernando Nogueira de Sá[a], Emilio Carlos Nelli Silva[a,*]

Department of Mechatronics and Mechanical Systems Engineering, School of Engineering, University of São Paulo, SP, Brazil

ARTICLE INFO

Article history:
Received 8 June 2022
Revised 8 September 2022
Accepted 13 September 2022
Available online 17 September 2022

Keywords:
Absorbing Layers
Hyperelliptical Absorbing Layers
Hybrid Absorbing Boundary Conditions
Semi-infinite media
Infinite media
Inverse problems

ABSTRACT

Modeling unbounded or semi-infinite media with numerical methods, such as finite elements, requires avoiding that waves pass through the boundaries of the truncated computational domain without reflection. For this reason, in areas such as Geophysics or Acoustics, absorbing layers are used to circumvent this issue. Nevertheless, sizing them is an open problem due to the necessary calibration of their parameters for an adequate performance and to prevent numerical instabilities. Absorbing layers are dependent on both wave frequency and material properties set up inside them and, affect the convergence of iterative methods in inverse problems by the inherent variation of domain properties within the process, especially in the transient regime. On the other hand, hybrid absorbing boundary conditions are the combination of absorbing layers and the application of non-reflecting boundary conditions on the layer boundary with the purpose of increasing their effectiveness. In this work, an analytical approach is presented to size the portion added to the original domain and to determine its damping parameters simultaneously. Hyperelliptical absorbing layers are introduced and, for generating the hybrid absorbing boundary conditions scheme, Sommerfeld or 1^{st}-Higdon boundary conditions are imposed on the outer layer boundary. Therefore, this methodology is adaptive according to the intermediate solutions of the transient optimization process for reducing possible numerical instabilities and spurious information for the inverse problem. The transient equilibrium equations are implemented by using the finite element method and an implicit time integration method. Results are presented to show the potential of the proposal.

1. Introduction

In areas such as Geophysics or Acoustics, the simulation of waves propagation in an unbounded domain by using numerical methods requires special treatment for the boundaries of the truncated computational domain so that waves should pass through truncated domain boundary without reflections. In this way, numerical models can fit into computers with limited computational time and memory in order to mimic the infinite or semi-infinite domain. Thus, the boundary conditions (BCs) applied in this type of problems are named Absorbing Boundary Conditions (ABCs). Some requirements that ABCs should satisfy are: well-posedness, accuracy in both continuous and discrete level, compatibility and stability with the numerical method used, efficiency, and ease and generality of the implementation. However, in practice is extremely

* Corresponding author.
E-mail address: ecnsilva@usp.br (E.C.N. Silva).

https://doi.org/10.1016/j.apm.2022.09.014
0307-904X/

Abbreviations

ABC	Absorbing Boundary Condition
AL	Absorbing Layer
AML	Automatically Matched Layer
BC	Boundary Condition
DoF	Degrees of Freedom
DGFE	Discontinuous Galerkin Finite Element
FD	Finite Difference
FDM	Finite Difference Method
FE	Finite Element
FEM	Finite Element Method
GABC	Generating Absorbing Boundary Condition
HABC	Hybrid Absorbing Boundary Condition
IC	Initial Condition
NRBC	Non-Reflecting Boundary Condition
PML	Perfectly Matched Layer
SEM	Spectral Element Method
SL	Sponge Layer
VOFM	Volume of Fluid Method

Symbol List

a	Layer major semi-axis
a_*	Adimensional propagation speed parameter
a_{C_R}	Coefficient for quadratic part in regression for computing minimum damping ratio
a_ξ	Coefficient for quadratic part in proposed damping function
A_{al}	Area of the model including the AL
A_H	Hyperelliptical domain area
A_{Hp}	Partial hyperellipse domain area
A_{orig}	Area of the original model without AL
A_R	Rectangular domain area
b	Layer minor semi-axis
b_{C_R}	Coefficient for linear part in regression for computing minimum damping ratio
b_ξ	Coefficient for linear part in proposed damping function
c	Propagation speed
c_{eq}	Equivalent propagation speed
c_{C_R}	Coefficient for constant part in regression for computing minimum damping ratio
c_{max}	Maximum propagation speed in the model
c_{min}	Minimum propagation speed in the model
C_R	Reflection coefficient
C_{Rmin}	Minimum reflection coefficient
C_{Rmin}^{FDM}	Spurious reflection coefficient for FDM
C_{Rmin}^{FEM}	Spurious reflection coefficient for FEM
C_{Rmin}^{QUA}	Minimum reflection coefficient for proposed quadratic damping function
C_{Rmin}^{RDF}	Minimum reflection coefficient for a given reference damping function
C_{Rmin}^{*}	Approximated optimized minimum reflection coefficient
c_Γ	Propagation speed at the boundary
d	Normalized element size
e_I	Integral error
e_P	Peak error
f	Linear frequency
f_E	Ellipse eccentricity
f_m	m-th linear frequency
f_{min}	Dominant frequency at the critical point at the boundary
f_{REF}	Reference frequency for calculating layer size
f_s	Source central frequency
F_A	Area factor
F_{A_H}	Hyperelliptical area factor

F_{GHM}	Fictitious correction factor by geometry for heterogeneous media
F_L	Domain fraction that must be added as an absorbing layer
F_R	Points for representing the central wavelength of the source
$F_{\omega *}$	Frequency factor for domains with absorbing layer
F_{ω_E}	Frequency factor for elliptical domains
F_{ω_H}	Frequency factor for hyperelliptical domains
F_{ω_R}	Frequency factor for rectangular domains
j	Imaginary unit
k	Wave number
k_a	Layer wave number
k_ω	Eikonal factor to estimate the natural frequency
l	Loss factor
l_{min}	Minimal dimension of the finite element
L	Length of the original domain in 1D models
L_a	Absorbing layer length in 1D models
L_s	Distance from the source to the point with ϕ_{min}
L_x	Domain length in the coordinate x
L_y	Domain length in the coordinate y
L_ξ	Absorbing layer length in 2D models
m	Vibration mode
n	Hyperellipse degree
n_{max}	Maximum hyperellipse degree
n_{min}	Minimum hyperellipse degree
n_*^{ari}	Hyperellipse degree calculated by arithmetic mean
n_*^{geo}	Hyperellipse degree calculated by geometric mean
n_*^{har}	Hyperellipse degree calculated by harmonic mean
N_{el}	Number of elements inside the layer
$N_{\Delta t}$	Number of time steps
p	Dimensionless wave number
R	Amplitude attenuation factor
R_A	Domain aspect ratio
R_{bc}	Initial boundary condition ratio
R_{eik}	Residual for the Eikonal equation
R_F	Frequency factor ratio
s	Hyperellipse *superness*
t	Time
t_a	Time spent for a wavefront to travel the layer
t_f	Final time for the simulation
u	Vibration amplitude
u_0	Initial disturbance
$u^{Pk\max}$	Maximum peak observed in the time response
v_p	Approximated speed propagation
x_i	Reference distance based on the original domain centroid
x_i^{crit}	Coordinates for the critical point
x_i^{REF}	Reference distance based on the original domain boundary
x_i^{ξ}	Point inside the absorbing layer
$x_i^{\Gamma_D}$	Nearest point that belongs to the boundary of the original domain
X_{C_R}	Heuristic factor for computing minimum damping ratio
$X_{C_R}^{ini}$	Initial heuristic factor for computing minimum damping ratio
$X_{C_R}^{max}$	Maximum heuristic factor for computing minimum damping ratio
$X_{C_R}^{min}$	Minimum heuristic factor for computing minimum damping ratio
$X_{C_R}^{\mathrm{FEM}}$	Heuristic factor for computing minimum damping calculated from FEM reflection coefficient
$X_{C_R}^{\mathrm{MDF}}$	Heuristic factor for computing minimum damping calculated from FDM reflection coefficient
$X_{C_R}^{\mathrm{RDF}}$	Equivalent factor for estimating minimum damping ratio
$X_{C_R}^{*}$	Approximate optimized factor for computing minimum damping ratio
γ	Complex wave number

Γ_D	Original domain boundary
Γ_L	Layer domain boundary in unidimensional model
Γ_ξ	Outer absorbing layer boundary
Δt	Time step size
Δt_{max}	Maximum time step size
ε_i	Spurious reflection rate due to the imposition of discretized boundary conditions
η	Damping coefficient
η_{cr}	Critical damping
θ_1	Angle between the normal of the surface and point on the boundary
λ_s	Source central wavelength
μ_{eik}	Pseudo-viscosity to smooth the solution in the Eikonal equation
ν_ξ	Proposed damping function inside the layer
ξ	Damping ratio
ξ_{max}	Maximum damping ratio
ξ_{min}	Minimum damping ratio
ϕ	Arrival time
ϕ_{min}	Minimum arrival time
ϕ_Γ	Boundary arrival time
ω_n	Angular natural frequency
ω_{1REF}	Approximated fundamental frequency for model without absorbing layer
ω_1	Fundamental frequency
Ω	Original truncated domain
Ω_ξ	Absorbing layer domain

difficult [1]. Detailed information and comparisons about all types of ABCs can be found in the reviews of Tsynkov [2], Bérenger [3], Cohen [4], Givoli [5], Gao *et al.* [6] and, Pled and Desceliers [7].

Two solutions have been suggested for ABCs: Non-Reflecting Boundary Conditions (NRBCs) and Absorbing Layers (ALs) [8]. NRBCs are boundary conditions applied on the artificial domain boundary ("original" computational or truncated domain boundary) that try to avoid reflections back to it without adding more material. Their most important characteristics are: wave directionality, wave dispersion and, generation and absorption of waves [9]. While ALs are an alternative to NRBCs where the domain of interest is surrounded by some artificial material in which waves are trapped and attenuated. However, the modeling of these layers is an open problem since they are described by attenuation functions with parameters that require proper calibration in any approach, and sometimes it may present numerical instabilities [4,10].

Two types of ALs are distinguished: Perfectly Matched Layers (PML) and Sponge Layers (SL). In PML, the idea is perfectly matching the impedance between media involved in the problem with the purpose of generating no reflection at the interface between them, independent of the angle of incidence and frequency of the waves. Some alternatives based on the same concept match the impedance of the absorbing medium with that of vacuum [11,12]. While in SL, dissipative terms are added to the governing equations to damp the outgoing waves, which requires prior information about their frequency and direction of propagation to setup damping parameters [10,13]. SL are simple and easy to implement [14] performing well for waves at grazing incidence and being less effective at normal incidence [15]. However, large layer sizes are required for low-frequency reflections.

The pioneering works in ABCs for transient problems model electromagnetic wave propagation by using the Finite Difference Method (FDM), and address the issue as radiating boundaries by using a Sommerfeld BC on the boundary of an added layer to the original domain [16,17]. Nonetheless, the concept of PML is considered to have been introduced with the Bérenger's work [12] in electromagnetic wave simulation. The PML formulation is obtained by extending the wave equation in the complex domain and causing the division of a real field into two nonphysical fields [13]. However, this modification adds new variables so that the computational cost is increased. Recently, Bériot and Modave [18] introduce the Automatically Matched Layer (AML) for convex domains with regular or irregular boundaries. The mesh is extruded according to the element geometry and a local curvilinear coordinate system as used by Modave *et al.* [19]. Despite this, the thickness and the desired reflection coefficient greater than zero must be provided by the user.

The sponge layer (or Gaussian taper boundary condition) was proposed by Cerjan *et al.* [14] in the context of FD modeling of acoustic and elastic wave propagation in the time domain. The method is based on a progressive reduction of the vibration amplitudes by using a decaying exponential function in the direction perpendicular to the layer boundary. In addition, the layer size is increasing at the edge opposite for the case of the presence of a free surface boundary. Larsen and Dancy [20] perform a similar process by dividing gradually the state variables by a factor governed by an exponential function that depends on both the SL size and the grid size. Rodrigues and Dimitrovová [21] propose an SL by using the Caughey AL method comparing with different damping profiles including an exponential one. Recently, Ma *et al.* [22] use an SL with mass-proportional damping in elastic waves for peridynamic problems.

Traditionally, Dirichlet BCs have been used on the end of AL [23–25]. However, Petropoulos had shown that for PML layers this BC is not important if the damping profile is linear or quadratic, and the layer is not thin [26]. Nevertheless, in this same work, it was observed that a layer with tuned NRBC may produce about half the spurious reflections that those with a traditional BC. Furthermore, the results of Collino and Monk show that by using an NRBC on the layer boundary together a quadratic loss profile inside the layer reduces the reflection coefficient for waves close to normal incidence [27]. Lately, Bériot and Modave [18] apply a Neumann BC on the outer layer boundary.

Regardless of the type of AL, modifying the original domain by adding degrees of freedom to the model has been a computational cost concern since the beginning [11,28–31]. Besides, considering the various approaches to PML, this can be more problematic because of the number of auxiliary variables required according to the formulation [31,32]. Nonetheless, thin layers have a rapid variation of damping or loss parameters that can cause numerical instabilities [13].

On the other hand, NRBCs are based on approximations of pseudo-differential operators with the aim of generating one-wave equations with non-reflective effects on artificial boundaries [33]. Although they are cheaper than AL from the computational point of view, these NRBCs are perfectly absorbent only for a range of angles of incidence [34,35]. In addition, the error introduced into the model by this type of BC is inversely proportional to the distance from the source to the artificial boundary raised to the order of approximation [2,8]. Thus, NBRCs are exact if the error tends to zero when the order increases, otherwise it is asymptotic [5]. Nevertheless, increasing the order means implementing high-order derivatives that can lead to numerical instabilities. For this reason, in practice, low-order are used [1].

In recent times, Modave *et al.* [36] formulate high-order NRBCs in a DGFE implementation for acoustic waves in 3D cuboidal domains and compatibility in corners and edges for avoiding numerical instabilities. However, additional 0D, 1D, 2D, and 3D equations must be solved due to the compatibility. Recently, in the field of fluids, Wellens and Borsboom [9] presented a Generating Absorbing Boundary Condition (GABC) for simulating free-surfaces by using Volume of Fluid Method (VOFM), which has the peculiarity of absorbing the outgoing waves and radiating the incoming waves. Gordin *et al.* [37] use a rational approximation for an NRBC for transverse vibrations in rods to minimize the additional calculations at every time step in FDM.

However, despite the vast literature on NRBCs, no good solution to the problem has been found and the proposed solutions work reasonably well. This is because the higher the accuracy, the higher the growth of low-frequency modes. [15]. Despite this, NRBCs based on Higdon BC [35,38] are widely used in both FEM [39–41] and FDM [42,43] and, although it requires auxiliary variables to implement high-order conditions, it has been shown to be stable [44].

An essential aspect to obtain the best performance of the ALs is the selection of parameters. Bérenger [12] had already perceived that regardless of the set of parameters of the AL, reflections always occur in numerical models of unbounded and semi-infinite media. A portion of these reflections being spurious because of the discretization itself and the imposition of boundary conditions [45,46]. However, tuning parameters allows to reduce them and improve the accuracy [36], especially increasing the layer size [12,18,47]. Constant damping or loss factor within AL originates a strong numerical reflection in the interface between the truncated domain and the layer [12]. Thus, damping or loss profiles play an important role in minimizing reflections since the inadequate selection of distribution functions and their parameters may cause discontinuities or an increase of the field strength [48]. Furthermore, these parameters depend on the frequency and the discretization [49]. However, there is no criterion for selecting the maximum damping or loss factor and, by using larger values for it, discretization errors may be dominant [24].

Several damping or loss profiles have been used inside ALs with the purpose of minimizing the reflections. In the preliminary works on PML, Holland, and Williams [11] determined by trial and error that a quadratic profile presents a good performance in electromagnetic waves while Bérenger [12] used constant, linear and quadratic, obtaining better results with the quadratic ones.

In the case of PML approaches implemented in FEM, in addition to the classic quadratic [23,46] profile, other ones have been used such as: cubic [18], quartic [46], hyperbolic polynomial [18,19,24,50] and shifted hyperbolic polynomial [19]. In relation to SL, damping or loss profiles are also varied in the literature. Among them, it can be found implemented in FEM uses constant, linear, quadratic and cubic profiles [21,22,51]. However, special profiles such as half Hanning window function [51] (used in signal processing) and exponential with rational arguments [21] can be found.

The AL size of the layer must be selected properly since large layers increase severely the computational cost. Merewether [16] reports that a sufficient size for this layer is half the largest dimension of the original domain. This criterion is also used by Holland [17]. Cohen [4] states that one or two wavelengths for PMLs are sufficient for the reflection coefficient to be of the order of the dispersion of the numerical method while Shen and Giurgiutiu [51] recommend more than two wavelengths to ensure effectiveness. Nevertheless, Turkel and Yefet [13] mention that PMLs with lengths of around 8 grid points are common in practice. Conversely, Cerjan *et al.* [14] suggest the use of 20 grid points in SL-based FDM. Most of the criteria found in the literature for sizing ALs are based on reflection coefficient relations at the layer end assuming normal incidence [12,18,23,27,46,52–54]. Thus, a reflection coefficient and a maximum damping or loss factor are set up to find the corresponding layer size. However, the reflection coefficient can never be null since the expressions for sizing layers depend on its logarithm; therefore, the size function is asymptotic and, very large sizes can be obtained for reflections very close to zero.

Another factor that influences layer size is wave frequency. For electromagnetic waves, source frequencies found in the literature can vary between tens of MHz and GHz and layer sizes oscillates between 4 and 10 grid points for FDM [12,16,27,28,55]. In the case of acoustic waves, the frequencies of the sources found are between tens of Hz and

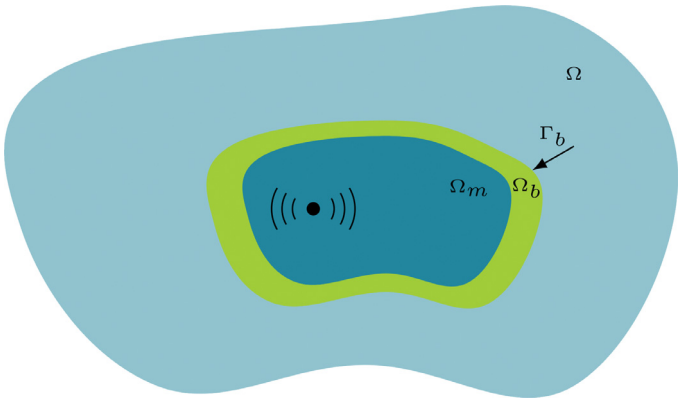

Fig. 1. Hybrid absorbing boundary conditions applied to an infinite medium.

kHz and layer sizes oscillates between 3 and 30 grid points for FDM [53,56–59], and between 2 and 10 elements for FEM [18,19,24]. Finally, for elastic waves, source frequencies between 1 kHz and 10 kHz and sizes between 10 and 20 either FDM grid points or FE [29,46,60], and ones of 2 spectral elements of polynomial degree 5 (*i.e.*, 11 Gauss–Lobatto–Legendre grid points) in SEM [23] are used. In addition, for different frequencies in the same problem, the AL Degrees of Freedom (DoF) can be maintained unchanged if the wavelength to element size ratio is constant [51]. Nonetheless, the layer size increases inversely as lower reflection coefficients are required due to numerical dispersion [27,46].

Some works have tried to optimally parameterize the AL [21,25,27,51], despite their dependence on material parameters, frequency, and incidence angles. Instead, the optimizations in NRBCs have been focused on the FDM coefficients for maximizing the boundary absorption [61] or the analytical coefficients of the NRBC for minimizing the reflection [9]. This hinders the convergence of iterative methods in inverse problems due to the variation of domain properties within the process, especially in transient regime. Consequently, the eigenvalues and the eigenvectors can change abruptly in the initial iterations; thus, the damping properties.

Hybrid Absorbing Boundary Conditions (HABCs) can be understood as the combination of the AL and the application of NRBCs on the AL boundary with the purpose of increasing their effectiveness [13]. Thus, the damping inside AL attenuates both the outgoing waves and reflecting ones by the boundary [62]. Furthermore, they can suppressed the low-frequency growing modes [15]. Some approaches have combined as a weighted sum the original wave equation with differential operators equivalent to one-way wave equations, such as Clayton-Engquist [34] and Higdon [35,38]. The weighting weights can be calculated through linear [31,63] and non-linear functions [64]. Other approaches have combined the radiation condition with a damping zone (*i.e.*, an AL) of quadratic damping profile to deal with nonlinear irregular wave problems [65].

In inverse problems, the ALs are not considered adaptive and can negatively influence the final result since the material distribution is changing with each iteration (especially in the first iterations). On the other hand, it is difficult to measure the efficiency of ALs in the transient regime and selecting the appropriate HABC parameters given a wide range of formulations. Moreover, pure NRBCs applied on boundaries of the computational domain can result in numerical instabilities and, ABC approaches such as PML or high-order Higdon-based BCs can result in an increase in the problem size by adding new variables due to formulation or implementation. Thus, it is necessary to develop a generic, systematic, efficient, and robust methodology for simulating infinite/semi-infinite media by using a hybrid approach (adaptive ALs combined with NRBCs on boundaries, see Fig. 1) in a transient regime, which can be used in order to solve the inverse problem.

In this work, a hybrid absorbing scheme is proposed consisting of a hyperelliptical absorbing layer combined with a non-reflecting boundary condition on the outer boundary with the purpose of reducing the artificial wave reflection when simulating unbounded or semi-infinite media. The AL size for bidimensional domains is determined according to an analytical formulation based on a unidimensional free vibration problem and the coefficient reflection for the passage of an incident wave from one material medium to another. Hyperelliptical layers with criteria-selected degrees are introduced as an alternative to traditional rectangular layers with the purpose of saving computational cost. Concerning to NRBCs, Sommerfeld or 1^{st}-Higdon BCs are imposed on the outer layer boundary in order to increase the AL performance and generating the HABC scheme. An adaptive quadratic damping profile with a criterion for the minimum damping is proposed and compared to some profiles proposed and found in the literature. This approach to bound the damping is opposite to the typical ones found in the literature, in which the maximum damping is usually selected. In addition, two propagation speed extension profiles inside the layer are studied: by circular sectors with respect to the source position and by straight continuity using the original truncated domain boundary as a reference. Transient equilibrium equations are solved by using the Finite Element Method (FEM) and an implicit time integration method, implemented in the FEniCS framework [66]. Therefore, a semi-infinite medium is simulated to observe the behavior of the dimensioned AL and find the optimized parameters that affect as little as possible the original problem. The proposed process can be applied to any phenomenon governed by the scalar wave equation.

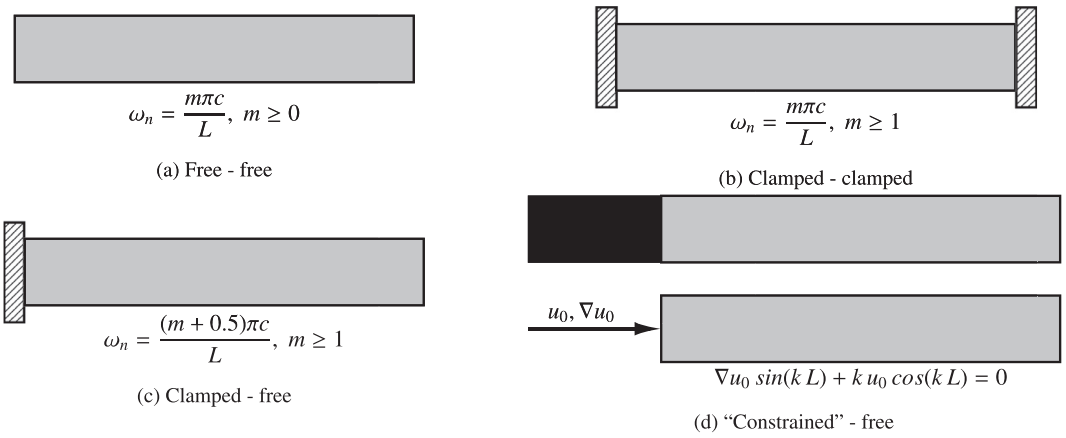

Fig. 2. Natural frequencies in bars for different BCs.

This work is organized as follows. In Section 2, the HABC scheme is presented discussing the proposed adaptive approach, determining the layer size and damping parameters from a unidimensional model as well as estimating its performance. Besides, the new layer shape for bidimensional domains is shown along with the strategy for NRBCs on its boundary. In Section 3, the numerical implementation is detailed. In Section 4, numerical examples are displayed including a unidimensional model for the purposes of verification and validation of the methodology and two bi-dimensional models to show the potential and performance of the proposed approach. Finally, in Section 5, concluding remarks are presented.

2. Hybrid Absorbing Boundary Conditions

Hybrid Absorbing Boundary Conditions (HABCs) are the combination of ALs with NRBCs on the added layer boundary (Fig. 1). Traditionally, Dirichlet BCs have been used at the end of the layer [23–25]. However, it is possible to improve the AL performance by imposing known NRBCs [13] such as Sommerfeld [13,67] or Higdon [35,38]. In this work, an analytical approach is presented to size the portion added to the original domain and to determine the required damping parameters simultaneously. This formulation is derived from unidimensional formulations and can be extrapolated to bidimensional ones with certain uncertainty and with some adjustments and corrections as will be seen later. Therefore, rectangular layers can be included in the original numerical model. However, it is possible to reduce the computational cost parameterizing the rectangular shape through of a hyperelliptical curve [68] and selecting a suitable curve degree. After that, either Sommerfeld or 1^{st}-Higdon BCs are imposed on the outer layer boundary for completing the HABCs approach. It should be highlighted that the AL is dimensioned assuming free vibration. Nevertheless, the methodology can be applied to any problem governed by the scalar wave equation, be it forced or not.

2.1. Adaptive HABCs Approach

The adaptive approach is based on the calculus of the AL size by analyzing and extrapolating to 2D models the behavior of a unidimensional bar in free vibration starting from the rest. The parameters of the AL are computed considering a free-free bar (Fig. 2a) to facilitate the calculations, especially the one related to the natural frequency.

Natural frequencies in bars for different BCs are shown in Fig. 2. It should be noted that for the free-free condition, the vibration modes start at $m = 0$, which corresponds to the rigid body motion due to the absence of constraints. For the case "constrained"-free, natural frequencies are calculated by solving a transcendental equation [69] (see Fig. 2d). The unidimensional problem for the proposal on HABCs could be approximated by the "constrained"-free bar. However, seeking the natural frequencies is not trivial because of the transcendental equation for their calculation. Considering the state variable u as the wave vibration amplitude and k as the wave number and, according to ratio between the initial BCs $R_{bc} = \frac{\nabla u_0}{k u_0}$ in left end in Fig. 2d, "constrained"-free bar could be approximated to a clamped-free bar ($R_{bc} \to \infty$) or a free-free bar ($R_{bc} \to 0$).

Now, considering the AL far enough from the source of disturbance, it can be modeled as a free-free bar for the approximate determination of its natural frequencies. Comparisons of the natural frequencies between a free-free bar and a free-Sommerfeld BC one show differences less than 0.02% (see Appendix A), so it can be concluded that the frequencies can be estimated without computational effort through the behavior of the free-free bar.

If an initial vibration amplitude is known, the approximate time response of the damping layer is estimated since constants depending on boundary conditions are determined. However, in a numerical model, it is necessary a boundary condition to avoid instabilities in the solution due to ill-conditioning systems. For this reason, a Sommerfeld or radiation boundary condition [13,67] for generating semi-reflecting boundaries on unbounded domains [4] is used on the outer layer boundary.

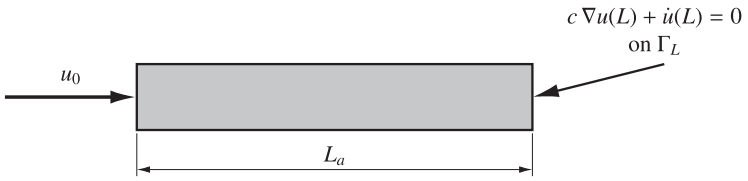

Fig. 3. Unidimensional model for the numerical study of HABCs.

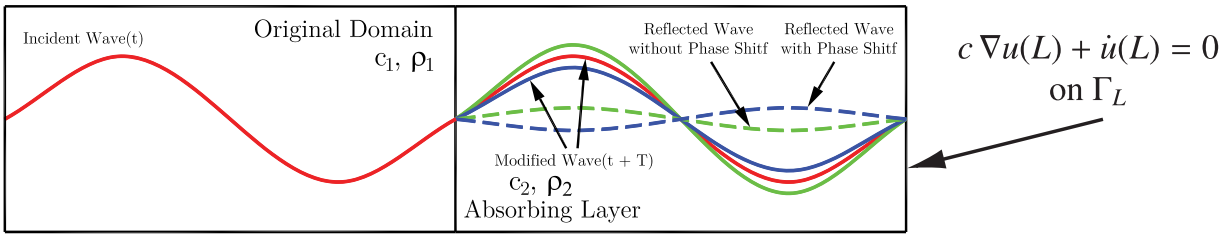

Fig. 4. Reflections due to material transitions.

This boundary condition is expressed by [1,9]:

$$c\nabla u \cdot \hat{n} + \dot{u} = 0 \text{ on } \Gamma_L \times (0, T) \tag{1}$$

with c as the propagation speed and Γ_L as the domain boundary where the Sommerfeld BC is applied. Therefore, the model in Fig. 3 for the numerical study of HABCs with an optimized length of ALs is considered in this research.

Another important topic is the imposing of material properties inside the AL. Consider the original domain and adjacent AL with a BC in the right end of Fig. 4. The incident wave will be reflected in a fraction of itself when it reaches the boundary between the original domain and the AL, and the reflection coefficient for the passage from a material medium to another can be calculated as [70] (Fig. 4):

$$C_R = \frac{k_1 - k_2}{k_1 + k_2} = \frac{c_2 - c_1}{c_2 + c_1} \tag{2}$$

with $k = \frac{\omega_n}{c}$. Later, the refracted or transmitted wave will reach the end where the BC is imposed, generating a new reflected wave causing constructive or destructive interference in the next incident waves. Remembering that the hypothesis of modeling is based on the scalar wave equation. That is, $\nabla u \lll 1$ [71], and so the density does not appear in the governing equations.

Thus, the reflections can be avoided at the interface between the original domain and the AL, imposing the same material properties in adjacent regions. That is, $C_R = 0$ if $c_1 = c_2$ (implying that the densities of the two mediums are also the same). For the attenuation of waves reflected because of the boundary conditions applied on the end of the domain, the damping properties should be appropriate according to the size of the AL. Moreover, the adoption of NRBCs on the boundaries of ALs also allows minimization of the reflections. The combination of these strategies originates the HABCs.

2.2. Size of AL

Considering the damped free vibration problem for the unidimensional bar with length L_a in Fig. 3 and without considering the Sommerfeld BC in the right end:

$$\begin{aligned} &\ddot{u} - c^2\nabla^2 u + \eta\dot{u} = 0, && \eta = \xi\,\eta_{cr} \\ &\text{ICs: } u(0,0) = u_0, && \dot{u}(0,x) = 0 \\ &\text{BCs: } \nabla u(t,0) = \nabla && u(t,L_a) = 0 \end{aligned} \tag{3}$$

with η as the damping coefficient, $\eta_{cr} = 2\omega_n$ as the critical damping and $\xi = \frac{\eta}{\eta_{cr}}$ as the damping ratio. The general solution for this differential equation is:

$$\begin{aligned} &u(t,x) = u_0\,\tau(t)\,\nu(x) \\ &\text{Characteristic Eq.:} \quad \lambda^2 + \eta\lambda + \omega_n^2 = 0 \quad \text{(Time Function)} \\ &\text{Solution Ch. Eq.:} \quad \lambda = -\frac{\eta}{2} \pm \sqrt{\Phi},\ \Phi = \left(\frac{\eta}{2}\right)^2 - \omega_n^2 \end{aligned} \tag{4}$$

being $\tau(t)$ and $\nu(x)$ functions depending on time and position, respectively and, λ the root of the characteristic equation for the time function $\tau(t)$. The value of the discriminant Φ generates three types of solutions:

$$u(t,x) = \begin{cases} \text{underdamped} & \Phi < 0 \Rightarrow 0 < \xi < 1 \\ \text{critically damped} & \Phi = 0 \Rightarrow \xi = 1 \\ \text{overdamped} & \Phi > 0 \Rightarrow \xi > 1 \end{cases} \tag{5}$$

For the calculation of the speed propagation of the wave inside the bar, the dispersion relation is taken into account. This relation is expressed as [72]:

$$\omega^2 - j\,\omega\,\eta = c^2\gamma^2,\ \ \gamma = k - j\,l \tag{6}$$

with γ as the complex wave number, l as the loss factor, and j as the imaginary unit. Therefore, the approximated speed propagation modified by the dispersion relation is (see Appendix B):

$$v_p = \frac{\omega}{k} \approx \frac{c}{1 + \frac{1}{8}\left(\frac{\eta}{\omega}\right)^2} = \frac{c}{1 + \frac{1}{2}\left(\frac{\xi f_m}{f}\right)^2} \tag{7}$$

where f_m is the m-th natural frequency of the bar and f is the frequency at which the wave travels. As mentioned in the Section 2.1, $m = 0$ corresponds to the rigid body motion that will not be considered here. Thus, $m \geq 1$ for the determining of the size of the AL is considered. On the other hand, the time spent for a wavefront to travel the entire bar with length L_a taking into account the dispersion relation is $t_a = \frac{L_a}{v_p}$ and, the wave number is $k_a = \frac{\omega}{v_p}$. The idea is to investigate in Eq. 4, the amplitude of the solution in $x = L_a$ at $t = t_a$ under the initial amplitude u_o assuming $f = f_m$ and, verify the possibility of attenuating the response by means of the introduction of an amplitude attenuation factor $0 < R \leq 1$ defined by:

$$R = \frac{|\,u(t_a, L_a)\,|}{|\,u_0\,|} = \frac{|u_0\,\tau\,(t_a)\,\nu(L_a)|}{|\,u_0\,|} \tag{8}$$

If $R > 0$ means that the reflected vibrations will be attenuated for the same factor again when they reach the point where the initial excitation was applied (for a total approximate attenuation of R^2 in relation to u_0). However, these reflected waves may originate from constructive interference as commented in Section 2.1.

Considering Eq. 4 with $m = 1$ since the fundamental mode to be attenuated requires the highest ξ in relation to the remaining modes, the underdamped solution enables the wave attenuation by a factor of $0 \leq R \leq 1$ when completely crossing the AL (the phase shift depending on the damping ratio ξ and the vibration mode m, see Eq. B.4, Appendix B). Remembering that, $0 < \xi < 1$ always for avoiding the critically damped solution. The overdamped case allows complete wave attenuation for specific values for $\xi > 1$. However, for other values, the amplitudes are not attenuated completely when crossing the AL. That is, excessive damping makes the system very slow, requiring too much space for the wave to be dissipated. Hence, the overdamped solution is not the appropriate solution for attenuation in ALs. Finally, for the critically damped regime and any $m \geq 1$, then $R = 0$. However, the behavior of the wave changes for a special case that represents a singularity for both cases underdamped and overdamped. This is a closed solution for all vibration modes and any length L_a and it is also not either the proper solution for calculating the layer size.

Therefore, R depends on the adequate selection of the damping ratio in order to avoid undesirable reflections at the end of the layer. The underdamped vibration regime is selected for seeking the size of the AL since it is possible to impose functions along the layer for a progressive attenuation.

When determining the vibration regime for the wave attenuation, it is necessary to define the size of the AL. Here, a size parameter F_L, related to the size of the original domain, is introduced in the underdamped solution for this purpose. This parameter is discussed in the next section.

2.3. Methodology for Calculation of F_L

The length of the AL is parameterized in relation to a portion F_L of the original domain with dimension L. Thus, $F_L = \frac{L_a}{L}$ represents the domain fraction that must be added as an AL. The amplitude attenuation factor R (Eq. 8) as a function of F_L, the m-th vibration mode and the damping ratio ξ is (see Appendix B):

$$R = \left|\frac{u(t_a, L_a)}{u_0}\right| = \left|\exp\left(-\xi m\pi A\right)\quad\left(\cos\left(m\pi A\sqrt{1-\xi^2}\right) + \frac{\xi}{\sqrt{1-\xi^2}}\sin\left(m\pi A\sqrt{1-\xi^2}\right)\right)\cos\left(\frac{2\pi F_L}{a_*}A\right)\right| \tag{9}$$

$$\text{with}\quad A = 1 + \frac{1}{2}\left(\frac{\xi m a_*}{2F_L}\right)^2\quad\text{and}\quad a_* = \frac{c}{fL}$$

The analysis of Eq. 9 shows that the fundamental mode ($m = 1$), to be attenuated in a factor R in an AL of length L_a, requires the highest $\xi < 1$ in relation to the remaining modes. Likewise, the fundamental mode to be attenuated requires the longest AL concerning the other modes considering the largest $\xi \to 1$. Therefore, the fundamental mode and $\xi = 0.999$ will be considered as a reference for calculating the size of the AL.

Fig. 5 presents two examples (solid lines) for $L = 1.2\ km$ and $c = 1.5\ ^{km}/_{s}$ at two different frequencies $f = 2.25\ Hz$ and $f = 5\ Hz$. It can be noted that, by requiring $R = 0$, the portion F_L (zeros of the function R) of the original domain increases with decreasing frequency. That is, the wavelength is longer, so more space is required to dissipate the wave considering the same damping ratio $\xi = 0.999$. On the other hand, the magnitude of the reflection coefficient $|C_{Rmin}|$ at the interface between the original domain where no damping is imposed and the AL with $\xi = 0.999$ is determined by (see Appendix B):

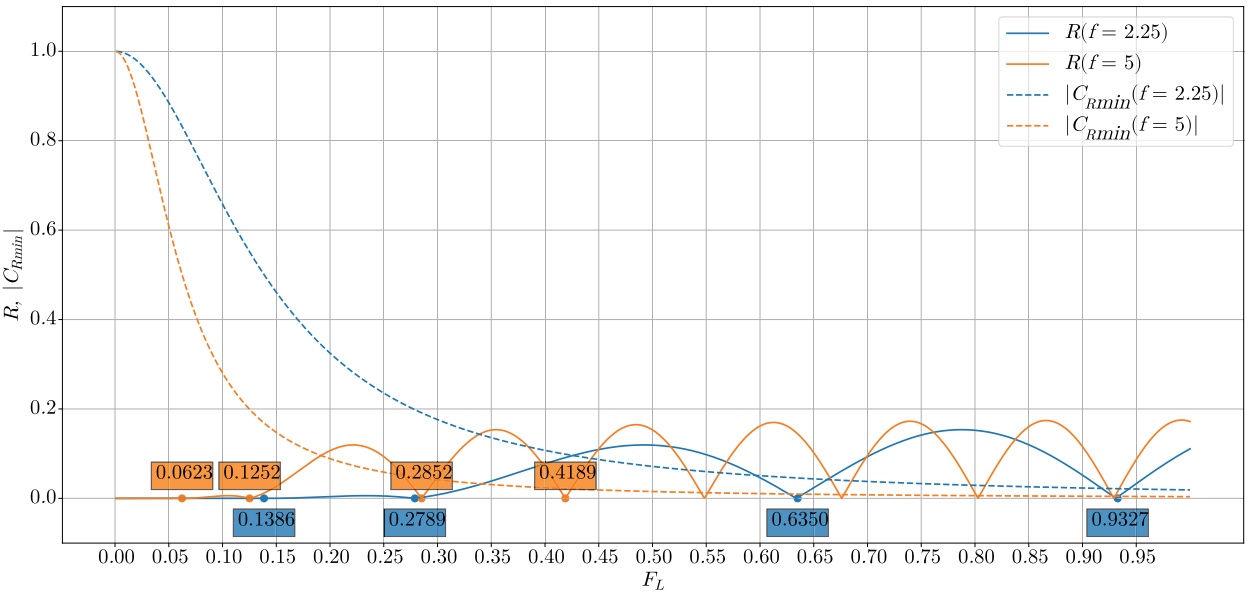

Fig. 5. Amplitude attenuation factor R (solid lines) and Minimum reflection coefficient $|C_{Rmin}|$ (dotted lines).

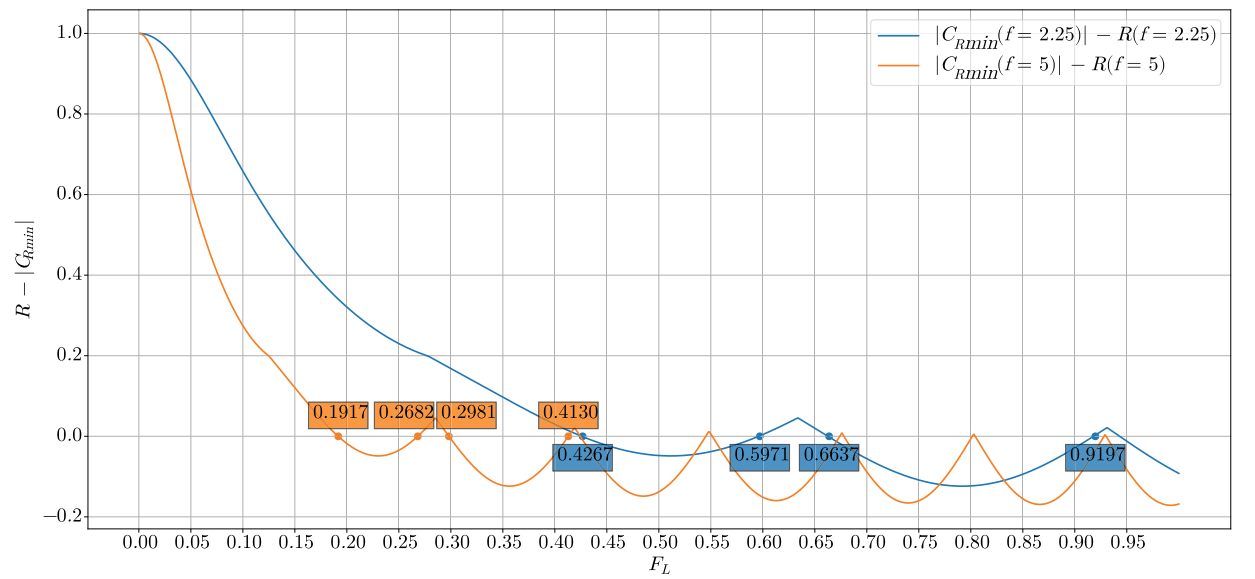

Fig. 6. Graph of the function $|C_{Rmin}| - R$. The zeros of the function represent the possible size F_L of the AL.

$$|C_{Rmin}| = \left| \frac{\xi^2}{\xi^2 + (4F_L/ma_*)^2} \right| \tag{10}$$

However, it is observed that when F_L is calculated with Eq. 10 may originate $F_L \geq 1$ (dashed lines in Fig. 5) when $|C_{Rmin}|$ tends to zero. That is, the portion F_L added to the domain is greater than the original domain. For instance, for the two frequencies considered before, if $|C_{Rmin}| = 0.001$ then $F_L = 1.974$ at $f = 5\ Hz$ and $F_L = 4.394$ at $f = 2.25\ Hz$. These calculated sizes make the implementation of an AL unfeasible. For this reason, the criterion proposed for selecting the proper AL size is based on finding the first root of the difference in the expression:

$$|C_{Rmin}| - R = 0 \tag{11}$$

Thus, F_L can reach values less than the original domain, although the higher F_L, the lower both R and $|C_{Rmin}|$. Fig. 6 shows the possible F_L for the frequencies considered in the previous examples. Coincidentally, $R = |C_{Rmin}|$ are the same for the frequencies considered previously and the first root found. Therefore, for $f = 5\ Hz$, $F_L = 0.1917$, and $f = 2.25\ Hz$, $F_L =$

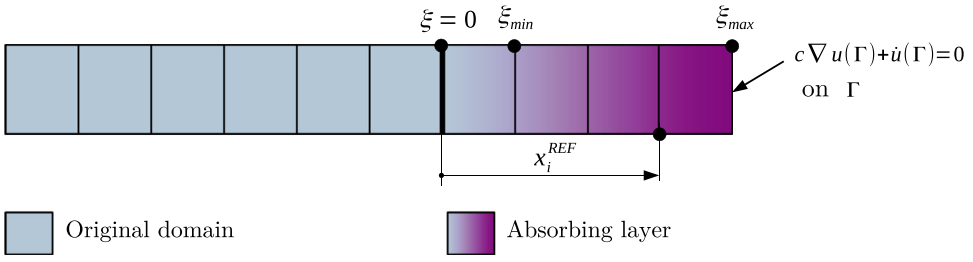

Fig. 7. Damping parameters for damping function ν_ξ. The applied NRBC (Sommerfeld in this case) on the layer boundary does not affect ν_ξ.

0.4267, the result obtained is $R = |C_{Rmin}| = 0.0960$. However, for bidimensional problems (see Sections 2.6 and 4.3), given that the reference length L is usually less than any original domain dimension and the medium can be heterogeneous, the appropriate size for the problem may be an n-th root of Eq. 11, always trying to select the smallest possible.

2.4. Damping Function for AL

The proposed function for the damping coefficient η inside AL is adaptive according to the number of finite elements N_{el} along it. The function is of the quadratic type depending on position and defined by:

$$\begin{aligned} \eta &= \eta_{cr}\nu_\xi = 2\omega_1\nu_\xi \\ \nu_\xi(x_i^{REF}) &= a_\xi\left(x_i^{REF}\right)^2 \quad + b_\xi x_i^{REF} \\ a_\xi = \frac{\xi_{min} - d\xi_{max}}{d^2 - d},\ b_\xi &= \quad \xi_{max} - a_\xi \end{aligned} \tag{12}$$

where $d = \frac{1}{N_{el}} \leq \frac{1}{2}$ to avoid division by zero (at least two elements must compose the layer), a_ξ and b_ξ are the coefficients of the function ν_ξ and, $x_i^{REF} = \frac{\|x_i^\xi - x_i^{\Gamma_D}\|}{F_L L}$ with $\|x_i^\xi - x_i^{\Gamma_D}\|$ as the distance between a point inside the AL and the nearest point that belongs to the boundary of the original domain (Fig. 7). Remembering that, the AL is dimensioned for the fundamental mode, then $\eta_{cr} = 2\omega_1$.

The extreme values for the damping ratio for $m = 1$ are:

$$\xi_{min} = \frac{\frac{4F_L}{ma_*}}{\sqrt{\frac{1}{|C_{Rmin}|} - 1}},\quad \xi_{max} = 0.999 \tag{13}$$

being ξ_{min} deducted from Eq. 10. Nevertheless, the function ν_ξ may be concave or convex with a maximum value $\nu_\xi > \xi_{max}$ inside the layer. Therefore, for ensuring that the vertex of ν_ξ is outside the layer (*i.e.*, $-\frac{b_\xi}{2a_\xi} \leq 0 \wedge -\frac{b_\xi}{2a_\xi} \geq 1$) and, $\nu_\xi \geq 0\ \forall\ x_i^{REF} \in [0, 1]$, the minimal damping ratio ξ_{min} must be satisfy the condition:

$$\xi_{max}d^2 \leq \xi_{min} \leq \xi_{max}\left(2d - d^2\right) \tag{14}$$

The magnitude of the reflection coefficient $|C_R|$ at any point inside the AL can be computed by (see Appendix B):

$$|C_R| = \left| \frac{\nu_\xi^2(x_i^{REF}) - \nu_\xi^2(x_i^{REF} - d)}{\left(\frac{4F_L}{ma_*}\right)^2 + \nu_\xi^2(x_i^{REF}) + \nu_\xi^2(x_i^{REF} - d)} \right| \tag{15}$$

The value for ξ_{min} (Fig. 7) that seeks to improve the performance of the HABCs can be estimated by:

$$\xi_{min} = X_{C_R}d \Rightarrow |C_R(\xi_{min})| = \left| \frac{(X_{C_R}d)^2}{\left(\frac{4F_L}{ma_*}\right)^2 + (X_{C_R}d)^2} \right| \tag{16}$$

where the term $X_{C_R} \geq 0$ is a heuristic factor determined by the user and remembering that $d = \frac{1}{N_{el}}$ (Eq. 12). Adjusting iteratively the parameter X_{C_R} (following the process shown in Section 3.4), it can be possible to obtain better performance against the layers traditionally considered (as seen in the results of Section 4). Numerical experiments in unidimensional models (Fig. 7) show that there is a value for X_{C_R} that maximizes the AL performance (see Section 2.5 for error measure definition). Nevertheless, a mathematical relationship could not be found to determine this value. Although X_{C_R} is unknown *a priori* and depends on the problem, extreme values can be determined to reduce the search space for the proper value in the iterative process. A minimum value $X_{C_R}^{min}$ can be obtained from the left side of Eq. 14 as:

$$\xi_{min} = \xi_{max}d^2 \Rightarrow X_{C_R}^{min}d = \xi_{max}d^2\ \ \therefore\ X_{C_R}^{min} = \xi_{max}d \tag{17}$$

Besides, the same numerical experiments show that a critical point of Eq. 15 is reached when $a_\xi = b_\xi$ in the proposed quadratic damping function (see Eq. 12). However, because of the circular dependency with d, it cannot be identified in advance as minimum or maximum of $|C_R|$. Despite this, an initial reference value $X_{C_R}^{ini}$ is determined as:

$$a_\xi = b_\xi \Rightarrow \frac{X_{C_R}^{ini} - \xi_{max}}{d-1} = \frac{\xi_{max}}{2} \;\therefore\; X_{C_R}^{ini} = \frac{\xi_{max}(1+d)}{2} \tag{18}$$

On the other hand, a maximum value $X_{C_R}^{max}$ is given by the right side of Eq. 14 in the equality condition so that:

$$\xi_{min} = \xi_{max}\left(2d - d^2\right) \Rightarrow X_{C_R}^{max} d = \xi_{max}\left(2d - d^2\right) \;\therefore\; X_{C_R}^{max} = \xi_{max}(2-d) \tag{19}$$

Another point of reference can be computed from the spurious reflection coefficient due to discretization. Recently, a spurious reflection coefficient for unidimensional FE that depends on the discretization is formulated as [73]:

$$\left|C_{Rmin}^{\text{FEM}}\right| = \left|\frac{(1-Z_1)\sin(p_1) + \dfrac{\alpha Z_2 - 1}{\alpha}\sin(\alpha p_2)}{(1-Z_1)\sin(p_1) - \dfrac{\alpha Z_2 - 1}{\alpha}\sin(\alpha p_2)}\right| \tag{20}$$

with $p_i = k_i \Delta x_i$ as the dimensionless wave number for i-th element with the wave number $k_i = \frac{\omega}{v_{pi}}$ and Δx_i as the length of the finite element, α as the length ratio between the elements involved in the calculation and, the terms Z_i defined by [73]:

$$Z_1 = \frac{\frac{1}{6}[\cos p_1 - 1]}{\frac{1}{3}[\cos p_1 + 1]} \quad \text{and} \quad Z_2 = \frac{\frac{1}{6}[\cos(\alpha p_2) - 1]}{\frac{1}{3}[\cos(\alpha p_2) + 1]} \tag{21}$$

In this work, p_1 ($\xi_1 = 0$) and p_2 ($\xi_2 = \xi_{min}$) are the dimensionless wave numbers for first and second elements of the AL (Fig. 7), $\Delta x = l_{min}$ is the minimal dimension of the finite element (Eq. 39), $\alpha = 1$ since the elements have the same size and v_{pi} is calculated as indicated in Eq. B.3 for $m = 1$ (Appendix B). Therefore, the dimensionless wave numbers for the first and second elements of the AL are expressed by:

$$p_1 = \frac{\omega}{c} l_{min} \quad \text{and} \quad p_2 = \frac{\omega}{c} l_{min}\left(1 + \frac{1}{8}\left(\frac{\xi_{min} a_*}{F_L}\right)^2\right) \tag{22}$$

However, to determine p_2 is necessary an initial guess for ξ_{min} ceases to be a circular dependency. This value can be computed from spurious reflection coefficient proposed for an open boundary condition in FDM [52]:

$$\left|C_{Rmin}^{\text{FDM}}\right| = \tan^2\left(\frac{k_1 l_{min}}{4}\right) \tag{23}$$

and the value for ξ_2 to determine p_2 is obtained from Eq. 10. The reflection coefficient computed with Eq. 23 is quite close to that calculated by Eq. 20, so it can be considered a good approximation. Then, another reference value is obtained from Eq. 16 by:

$$X_{C_R}^{\text{FEM}} = \frac{\frac{4F_L}{ma_*}}{d\sqrt{\frac{1}{|C_{Rmin}^{\text{FEM}}|} - 1}} \tag{24}$$

Therefore, three points are obtained from the previous analysis $\left(X_{C_R}^{ini}, \left|C_{Rmin}^{ini}\right|\right)$, $\left(X_{C_R}^{max}, \left|C_{Rmin}^{max}\right|\right)$ and $\left(X_{C_R}^{\text{FEM}}, \left|C_{Rmin}^{\text{FEM}}\right|\right)$ and since there is a minimum value for $|C_{Rmin}|$, these three points could be approximated by a quadratic function representing a convex parabola, so that its vertex indicates the desired value for X_{C_R}. Remembering that, reflection coefficients other than $\left|C_{Rmin}^{\text{FEM}}\right|$ are given by Eq. 16. The point $\left(X_{C_R}^{min}, \left|C_{Rmin}^{min}\right|\right)$ is not used in the regression because $\left|C_{Rmin}^{min}\right| \to 0$ causing bad numerical conditioning in it. The proposed parabola and the desired $X_{C_R}^*$ are:

$$|C_{Rmin}| = a_{C_R} X_{C_R}^2 + b_{C_R} X_{C_R} + c_{C_R} \quad \text{and} \quad X_{C_R}^* = -\frac{b_{C_R}}{2a_{C_R}} \tag{25}$$

and the details for the regression are shown in Appendix C. In practice, rounding errors due to the floating-point arithmetic and discretization errors when considering bidimensional elements lead to different values of $X_{C_R}^*$. Accordingly, an interval can be defined to limit its search based on the spurious reflection rates due to the imposition of discretized boundary conditions. These rates are defined as [45]:

$$\varepsilon_1 = |-1 + \cos p| \quad \text{and} \quad \varepsilon_2 = \left|\sin\frac{p}{2}\right| \tag{26}$$

where ε_1 corresponds to a Dirichlet BC while ε_2 resembles a Neumann BC and p is the dimensionless wave number. Here, $p = p_1$ with the purpose of calculating the spurious reflection rate assuming that the passage of medium with p_1 to one

with p_2 is between a Dirichlet BC and a Neumann BC. Thus, considering that ε_i is the percentage error in the computation of $\left|C^*_{Rmin}\right| = \left|C_{Rmin}(X^*_{C_R})\right|$ given by Eq. 25, the bounds of the interval for X_{C_R} by using Eq. 16 are:

$$\begin{aligned} X^{min}_{C_R} &= \max\left(\xi_{max}d, \frac{\frac{4F_L}{ma_*}}{d\sqrt{\frac{1}{(1-\min(\varepsilon_i))|C^*_{Rmin}|}-1}}\right) \\ X^{max}_{C_R} &= \min\left(\frac{\frac{4F_L}{ma_*}}{d\sqrt{\frac{1}{(1+\max(\varepsilon_i))|C^*_{Rmin}|}-1}}, \xi_{max}(2-d)\right) \end{aligned} \tag{27}$$

where $\left|C^*_{Rmin}\right| = \left|C^{ini}_{Rmin}\right|$ when $X^*_{C_R} < \xi_{max}d$. In the same situation, the minimum positive root of Eq. 25 is assumed as $X^{min}_{C_R}$ if it exists, otherwise $X^{min}_{C_R} = \xi_{max}d$ since $X_{C_R} \geq \xi_{max}d$ must be satisfied, that is:

$$\text{if } X^*_{C_R} < \xi_{max}d \Rightarrow X^{min}_{C_R} = \max\left(\xi_{max}d, \min\left(X^{min}_{C_R} : \frac{-b_{C_R} \pm \sqrt{\Phi_{C_R}}}{2a_{C_R}} > \xi_{max}d\right)\right) \tag{28}$$

with $\Phi_{C_R} = b^2_{C_R} - 4a_{C_R}c_{C_R}$. Summarizing, the initial guess is $X_{C_R} = X^*_{C_R}$ if $X^*_{C_R} \geq \xi_{max}d$, otherwise $X_{C_R} = X^{ini}_{C_R}$ and $X^{min}_{C_R}$ must be modified. Nevertheless, in bidimensional domains (see Section 2.6), taking into account that $\eta < \eta_{cr}$ depends on $0 < \xi < 1$ and ω_n (Eq. 3), and that the latter depends only on the geometry in homogeneous media [74], it could be expected that ξ_{min} would be affected by the aspect ratio of the domain R_A and the hyperellipse area factor F_{A_H} (Eq. E.3, Appendix E). Therefore, the proposed limits can be changed to modify the initially proposed interval so that:

$$X^{min}_{C_R} \leq X_{C_R} \leq X^{max}_{C_R} \Rightarrow \begin{cases} X^{min}_{C_R} = \max\left(\xi_{max}d, \frac{F_{A_H}}{4}\min\left(\frac{1}{\sqrt{1+R_A^2}}, \frac{R_A}{\sqrt{1+R_A^2}}\right)\frac{\frac{4F_L}{ma_*}}{d\sqrt{\frac{1}{(1-\min(\varepsilon_i))|C^*_{Rmin}|}-1}}\right) \\ X^{max}_{C_R} = \min\left(\frac{4}{F_{A_H}}\max\left(\sqrt{1+R_A^2}, \frac{\sqrt{1+R_A^2}}{R_A}\right)\frac{\frac{4F_L}{ma_*}}{d\sqrt{\frac{1}{(1+\min(\varepsilon_i))|C^*_{Rmin}|}-1}}, \xi_{max}(2-d)\right) \end{cases} \tag{29}$$

where the terms $\frac{F_{A_H}}{4}$ and $\frac{4}{F_{A_H}}$ are the area ratio between a hyperellipse and a rectangle with the same semi-axes and its inverse ratio, respectively. The terms as arguments in operators $\min(\cdot)$ and $\max(\cdot)$ are obtained from Eq. E.1 (Appendix E) considering the aspect ratio R_A and its inverse and retaining only the factors depending on itself and, likewise computing their inverses. That is, the arguments in $\min(\cdot)$ are the inverses ones in $\max(\cdot)$. Moreover, the same modifications for $\left|C^*_{Rmin}\right|$, $X^{min}_{C_R}$ and $X^*_{C_R}$ in the unidimensional case are applicable if $X^*_{C_R} < \xi_{max}d$.

Besides, reference values can be calculated by equaling the expressions for $|C_{Rmin}|$ of the proposed quadratic damping distribution and a known damping distribution acting as a reference. That is $\left|C^{QUA}_{Rmin}\right| = \left|C^{RDF}_{Rmin}\right|$, where the superscript *RDF* represents a given *Reference Damping Function*, $\left|C^{RDF}_{Rmin}\right|$ is obtained from Eq. B.6 (Appendix B) when the damping ratio ξ is expressed as a function of the position according to *RDF*, and $\left|C^{QUA}_{Rmin}\right|$ comes from Eq. 16. Thus, solving the above equality, a factor $X^{RDF}_{C_R}$ is found, *i.e.*, the equivalent factor based on the *RDF*. The functions used as a reference and the corresponding expressions for $X^{RDF}_{C_R}$ can be found in Appendix D. Remember that an allowable value to be used in Eq. 16 must satisfy $X^{min}_{C_R} \leq X^{RDF}_{C_R} \leq X^{max}_{C_R}$.

2.5. Layer Performance Estimation

The performance of the layer sized with the methodology proposed is estimated through the calculation of the errors. The error is computed at critical points according to a criterion based on the shortest arrival time at the original boundary named in this work as ϕ_{min}. The point on the boundary that suffers the first contact with the wavefront (at $t = \phi_{min}$) is critical to estimate the model error, since is most likely to receive reflections when an AL is added. Therefore, this will be where the error estimation will be computed. One way to determine this point is to use the Eikonal equation [75] with the purpose of finding the shortest time needed to travel from the sources to the boundary. The Eikonal is a nonlinear equation traditionally used to evolve interfaces [75] but it has also been used to find the distance to walls [76]. In this work, a hyperbolic Eikonal equation is used [77]:

$$|\nabla\phi| = \frac{1}{c} + \mu_{eik}\nabla^2\phi \tag{30}$$

where ϕ is the elapsed time to the wavefront, c is propagation speed in the medium, and μ_{eik} is a pseudo-viscosity to smooth the solution. However, a small conceptual change to the meaning of ϕ is needed. By setting $\phi = 0$ at the sources

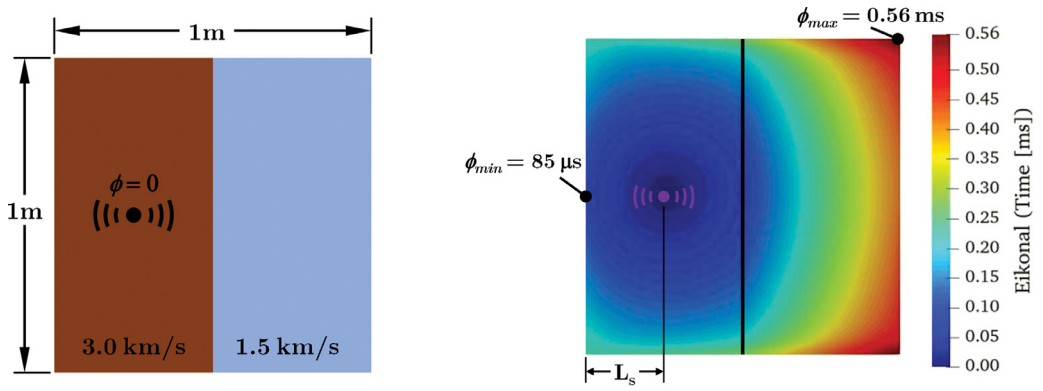

(a) Eikonal domain example.

(b) Time to reach the boundary.

Fig. 8. Eikonal example: Domain and time taken to reach boundary.

the calculated value of ϕ becomes the elapsed time for the wavefront to reach each point of the domain. Thus, the critical point with coordinates x_i^{crit} is determined by the minimum arrival time ϕ_{min} in the original model without any layer. Several points can be determined with this criterion if ϕ_{min} is measured on each boundary independently.

Figure 8 shows a small example of this feature. The source located in the centroid of the left region is set with a fixed $\phi = 0$ and two region with different propagation speeds are defined (Fig. 8a) and the time taken to reach the boundaries are shown in Fig. 8b. In this example, the critical point for the left side boundary would be the one that presents $\phi_{min} = 85\ \mu s$ and the distance from the source to this point is defined as L_s (see Fig. 8b). L_s is the base distance for the AL size calculation in bidimensional domains (see Section 2.6). After choosing the critical points, the AL efficiency is evaluated by means of an integral error e_I defined as [21]:

$$e_I = \frac{\int_0^{t_f} (u_{\text{MOD}} - u_{\text{INF}})^2 \mathrm{d}t}{\int_0^{t_f} u_{\text{INF}}^2 \mathrm{d}t} \tag{31}$$

and by a peak error e_P defined as:

$$e_P = \left| \frac{u_{\text{MOD}}^{Pk\max}}{u_{\text{INF}}^{Pk\max}} - 1 \right| \tag{32}$$

with u as the wave vibration amplitude at the critical point, $u_i^{Pk\max}$ as the maximum peak observed in the response in the time interval $t \in [0, t_f]$ at the same point. Subscripts MOD and INF refer to the model with AL and the reference one, respectively. The reference model is understood as a model with sufficient extension without any type of damping so that the effects of its boundaries do not influence the transient response of the original truncated model. It should be noted that it is desirable that the errors are as small as possible, *i.e.*, $e_I \to 0$ and $e_P \to 0$. The integral error e_I is the dominant efficiency factor because it takes into account the response in all time steps. However, in the case of a tie, the peak error e_P can define which size of AL is more adequate for the problem.

2.6. Adaptive HABCs for Bidimensional Problems

The methodology explained in this section is applicable to both complete and partial layers, that is, with some of their boundaries acting as a free surface (a Neumann BC is considered in this case: $\nabla u \cdot \hat{n} = 0$).

Rectangular layers are the classical ALs considered in regular domains whose corners are singularities that may originate undesirable reflections or numerical instabilities. Nonetheless, other shapes might be considered with the aiming of reducing the computational cost. Thus, hyperellipses are proposed as an intermediate solution between the reducing area of the layer and the accompanying radial propagation of the excitation. A hyperellipse is a closed curve defined by:

$$\left|\frac{x}{a}\right|^n + \left|\frac{y}{b}\right|^n = 1 \tag{33}$$

being n, a and b positive numbers. An ellipse is obtained when $n = 2$ while a rectangle is obtained when $n \to \infty$. Nevertheless, some points on its boundary can be closer to the corners of the original domain, making the AL less effective. On the other hand, larger ALs may be required for models with high propagation speeds, low wave frequencies, and sources close to boundaries. Thus, n could be increased by adding more material to the AL.

In this work, for bidimensional domains and complete layers, it is considered rectangular ALs with dimensions $(L_x + 2L_\xi) \times (L_y + 2L_\xi)$ and hyperelliptical ones with semi-major axis $a = 0.5L_x + L_\xi$ and semi-minor axis $b = 0.5L_y + L_\xi$. In the

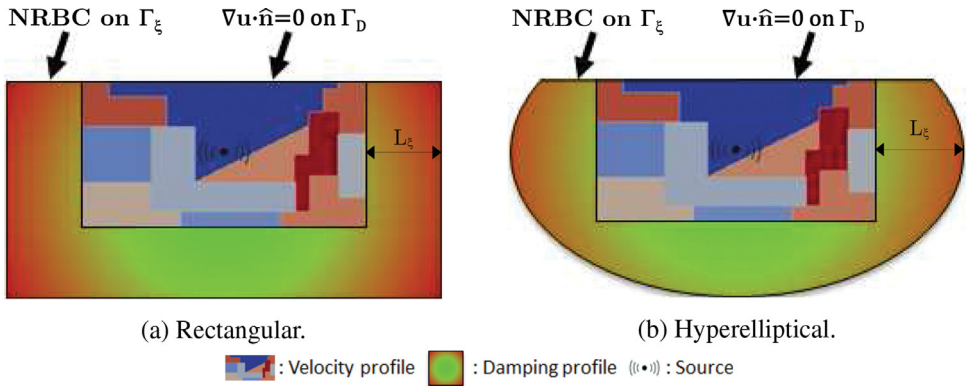

Fig. 9. Shapes of different ALs analyzed.

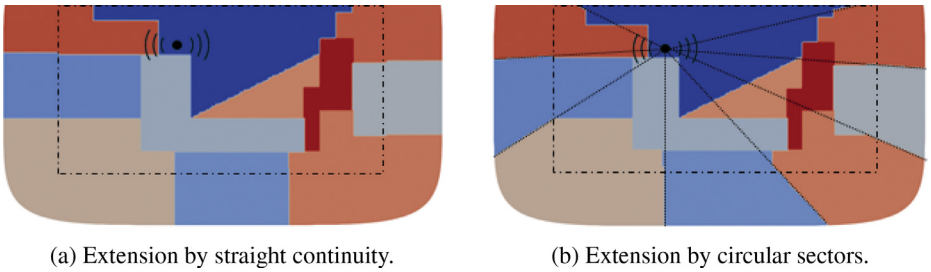

Fig. 10. Distribution of the speed propagation for bidimensional ALs.

case of domains with a top-free surface, it is considered rectangular ALs with dimensions $(L_x + 2L_\xi) \times (L_y + L_\xi)$ and hyperelliptical ones with semi-major axis $a = 0.5L_x + L_\xi$ and semi-minor axis $b = 0.5(L_y + L_\xi)$ (Fig. 9). Circular layers are intended to accompany the radial nature of the propagation of the excitation. However, their area is greater than the hyperelliptical ones and for this reason, they are not considered in this study.

The size parameter of AL is given by $L_\xi = F_L L_s$, where L_s is the distance from the source to the point belonging to the original boundary where ϕ_{min} is found (Fig. 8). On the other hand, F_L is calculated as if the domain were unidimensional as explained in Section 2.3 and the adimensional propagation speed parameter $a_* = \frac{c}{fL}$ in Eq. 9 is computed considered $\frac{c}{L} = \frac{1}{\phi_{min}}$ (Eq. E.10, Appendix E).

Another strategy proposed to increase the effectiveness of HABCs is the distribution of the propagation speed c in circular sectors with respect to the source inside the AL, as indicated in Fig. 10b. This strategy is proposed by taking advantage of the fact the wave propagation from the excitation is radial in nature. Moreover, the propagation speed in the AL is the same as those in the adjacent region of the original domain (Fig. 4).

ALs are ABCs with inherent reflections for waves with oblique incidence [9]. Additionally, bidimensional domains have vibrations and harmonics in two directions [78]. Thus, with the purpose of increasing their efficiency, two NRBCs are considered on the layer boundary (Fig. 9) defined as [6]:

$$c\nabla u \cdot \hat{n} + \cos\theta_1 \dot{u} = 0 \text{ on } \Gamma_\xi \times (0, T), \ \theta_1 = \begin{cases} 0 & \text{Sommerfeld BC} \\ \text{otherwise} & 1^{st}\text{-Order Higdon BC} \end{cases} \tag{34}$$

and θ_1 for 1^{st}-order Higdon BC is considered the angle between the normal of a straight surface according to the boundary and the imaginary line between the point on it and the source as seen in Fig 11a. Nevertheless, if $\cos|\theta_1| < \sqrt{2}/2$ (that is, $|\theta_1| > 45°$), $|\theta_1|$ is substituted by $90° - |\theta_1|$. The damping distribution is imposed according to presented in Section 2.4 and the limit values for X_{C_R} are given by Eq. 29. Furthermore, the aspect ratio of the domain (including or not the AL) is defined as $R_A = \frac{a}{b}$. An example of the proposed quadratic damping profile given by Eq. 12 is shown in Fig. 11b.

3. Numerical Implementation

3.1. Time-dependent Wave Equation

The implemented governing equation is the forced wave equation given by:

$$\ddot{u} - c^2\nabla^2 u + \eta\dot{u} = g(x_i, t) \tag{35}$$

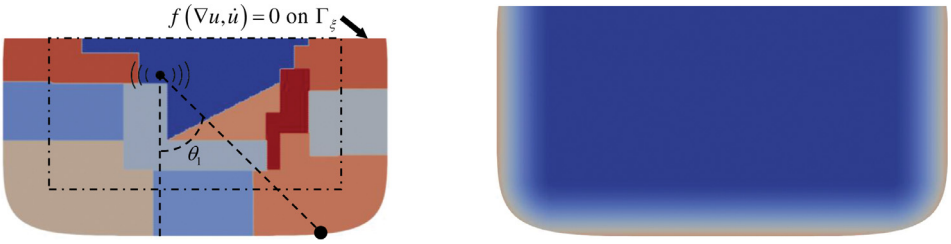

(a) Angle definition for the 1st-order Higdon BC. (b) Damping distribution proposed.

Fig. 11. Approaches considered for HABCs in bidimensional ALs.

highlighting again that, the proposed methodology for sizing ALs can be applied to forced or not problems. However, the AL is dimensioned assuming free vibration in a unidimensional problem (*i.e.*, $g(x_i, t) = 0$, as seen in Section 2.2). The proposed methodology is implemented in Python [79] aided by the FEniCS (based on FEM) [66]. An implicit time integration method is used for solving the weak form of Eq. 35 with an NRBC on the boundary (Figs. 1 and 9), starting from the rest, and discretized with backward FDM in time:

$$\begin{aligned}\int_\Omega \left(u^k - 2u^{k-1} + u^{k-2}\right)\cdot v\,\mathrm{d}\Omega + (\Delta t)^2 \int_\Omega c^2 \nabla u \cdot \nabla v\,\mathrm{d}\Omega + \Delta t \int_{\Omega_\xi} \eta\left(u^k - u^{k-1}\right)\cdot v\,\mathrm{d}\Omega_\xi \\ + \Delta t \cos\theta_1 \int_{\Gamma_\xi} c\left(u^k - u^{k-1}\right)\cdot v\,\mathrm{d}\Gamma_\xi = (\Delta t)^2 \int_\Omega g \cdot v\,\mathrm{d}\Omega\end{aligned} \tag{36}$$

where $u(x_i, t)$ is the wave vibration amplitude field, c is the wave propagation speed, $g(x_i, t)$ is the excitation, Δt is the time step size and v is an arbitrary test function. The third term in the first line integrated over the domain $\Omega_\xi \subseteq \Omega$ is the contribution of the added AL (being $\eta = 0$ in the original domain Ω). The first term in the second line integrated on the surface Γ_ξ is the NRBC on the AL boundary (Eq. 34). Remembering that in unidimensional domains, it is only applied a Sommerfeld BC (see Fig. 7). For bidimensional ones, the NRBCs considered in the layer boundary can be of the Sommerfeld or 1st-Higdon type. The system is always considered starting from rest, and when the excitation is required to be applied at one point in the mesh, a Dirac delta function in space and a time-dependent function $q(t)$ is used, so that:

$$g(x_i, t) = \delta\left(x_i - x_i^s\right) q(t) \tag{37}$$

with x_i^s as the source localization. Here, the source is a Ricker wave which is defined in the time domain as [80]:

$$q(t) = \left(1 - 2\left(\pi f_s\left(t - \frac{1}{f_s}\right)\right)^2\right) \exp\left(-\left(\pi f_s\left(t - \frac{1}{f_s}\right)\right)^2\right) \tag{38}$$

where f_s is the central or peak frequency and with maximum amplitude at $t = \frac{1}{f_s}$. On the other hand, the minimal dimension of the finite element l_{min} and the maximum value for the time step Δt_{max} are determined according to the expressions [81,82]:

$$l_{min} = \frac{c_{min}}{F_R f_s} \quad \text{and} \quad \Delta t_{max} = \frac{2 l_{min}}{\pi \sqrt{D} c_{max}} \tag{39}$$

where F_R is the number of points selected by the user for representing the central wavelength of the source $\lambda_s = \frac{c}{f_s}$ and, c_{min} and c_{max} are the minimum and maximum propagation speeds, respectively. D is the geometrical dimension of the model (unidimensional $D = 1$ or bidimensional $D = 2$). However, with purpose of conserving the same element size inside the AL, the size parameter F_L (see Sections 2.3 and 2.6) is rounded up with the ceiling function $\lceil \cdot \rceil$, so that:

$$F_L = \frac{l_{min}}{L_s} \left\lceil \frac{L_s}{l_{min}} F_L^{R=|C_{Rmin}|} \right\rceil \tag{40}$$

being $F_L^{R=|C_{Rmin}|}$ obtained from the methodology presented in Section 2.3 and with L_s as the reference distance as explained in Sections 2.5 and 2.6. In bidimensional problems, the maximum damping coefficient imposed inside the AL is based on the approximation of the fundamental frequency ω_1 of the bidimensional domain including the layer. The approximation of ω_1 depends on the minimum arrival time ϕ_{min} (see definitions in Sections 2.5 and 3.2) and geometrical considerations (see Appendix E). Remembering that, $\eta_{\max} = 2\xi\omega_1$ and $\xi = 0.999$. The analytical calculation of the fundamental frequency ω_1 for the hyperlliptical layers studied here are based on the approximations presented in [78,83,84] and, it is made in order to save computational effort. Besides, it is defined an area factor $F_A = \frac{A_{al}}{A_{orig}}$ that quantifies the increase in area when the layer is added with respect to the area of the original domain.

3.2. Eikonal Implementation

The Eikonal equation (Eq. 30) is used to find the point where the highest error should occur (see Section 2.5 for error measure definition). It is solved by using a finite element approach based on the Galerkin weak formulation with a linear

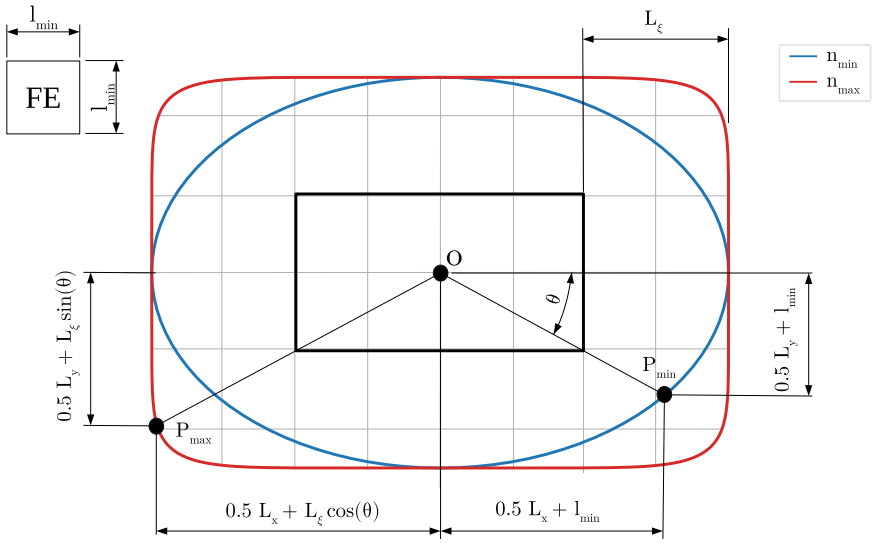

Fig. 12. Criterion for the minimum and maximum exponents (n_{min} and n_{max}) in hyperelliptical layers. l_{min} is the minimal dimension of the finite element (see Eq. 39).

interpolation. The weak form for the residual R_{eik} is given by [77]:

$$R_{eik} = \int_{\Omega} \sqrt{\nabla\phi \cdot \nabla\phi}\, y_e - \frac{f_e}{c}\, y_e + \mu_{eik} \nabla\phi \cdot \nabla y_e \, d\Omega - \int_{\Gamma} y_e \nabla\phi \cdot \boldsymbol{n} \, d\Gamma \tag{41}$$

where $f_e = 1$, y_e is a test function, and c is the propagation speed in the medium. It is assumed $\mu_{eik} = \sqrt{2} l_{min}$, *i.e.*, the maximal distance of two points in the FE. By setting a Dirichlet condition of $\phi = 0$ at the wave sources, and $\nabla\phi \cdot \boldsymbol{n} = 0$ at the boundaries, the calculated value of ϕ becomes the elapsed time for the wavefront to reach each point of the domain. Thus, the point on the boundary with the lowest value of $\phi = \phi_{min}$ becomes the point for the error evaluation. Besides, it is important to notice that the Eikonal is a non-linear equation, so the solution is found by minimizing the residual, so $R_{eik} \approx 0$ at the final solution.

3.3. Extreme Values for Hyperellipse Exponents

The minimum and maximum integer exponents (n_{min} and n_{max}) for hyperelliptical layers to be considered in the bidimensional analysis are defined from Eq. 33, so that they satisfy (Fig. 12):

$$\begin{aligned} n_{min} &: \left| \frac{0.5L_x + l_{min}}{a} \right|^{n_{min}} + \left| \frac{0.5L_y + l_{min}}{b} \right|^{n_{min}} \leq 1 \\ n_{max} &: \left| \frac{0.5L_x + L_\xi \cos\theta}{a} \right|^{n_{max}} + \left| \frac{0.5L_y + L_\xi \sin\theta}{b} \right|^{n_{max}} \leq 1 \end{aligned} \tag{42}$$

with the angle $\theta = \tan^{-1}(\frac{L_y}{L_x})$ and the remain terms defined in Section 2.6. That is, n_{min} is the minimum exponent for the hyperellipse that passes through or contains the point $P_{min} = (0.5L_x + l_{min},\ 0.5L_y + l_{min})$ considering the curve centered at the origin, *i.e.*, the projections on the semi-axes of the hyperellipse of the domain diagonal plus the diagonal of a finite element to avoid interference with the original domain. While n_{max} is the maximum exponent when assumed that the hyperellipse with the same center passes through or contains the point $P_{max} = (0.5L_x + L_\xi \cos\theta,\ 0.5L_y + L_\xi \sin\theta)$ where $L_\xi \cos\theta$ and $L_\xi \sin\theta$ are the projections of the parameter size L_ξ in the direction of the domain diagonal on the semi-axes of the hyperellipse, since $\theta = \tan^{-1}(\frac{L_y}{L_x})$.

n_{min} and n_{max} can be determined iteratively by evaluating the left side in both criteria of Eq. 42, so that the point that satisfies the equality is exactly on the boundary. On the other hand, as the exponents are considered integers if the value obtained on the left side is less than 1 the point is inside the hyperellipse and the exponent is accepted. Conversely, if it is greater than 1 the point is outside the curve and the exponent is rejected. However, n_{max} can be very large (*e.g.* a value of 6 or greater) with the proposed criteria, resulting in models that take a long time to evaluate and may be unnecessary, since as the exponent of the hyperellipse increases the system tends to have fewer differences with the rectangular layer model. Thus, an upper limit for n_{max} can be set up based on the *superness* concept. The *superness* s is a parameter that defines the extremal points ("corners") of a hyperellipse of degree n centered at the origin, so that [85,86]:

$$s = 2^{-(1/n)} \Rightarrow |x_{max}| = sa \wedge |y_{max}| = sb \tag{43}$$

then the extremal points are given by the coordinates $(\pm sa, \pm sb)$. Now, if it is considered that $P_{max} = (0.5L_x + L_\xi \cos\theta, 0.5L_y + L_\xi \sin\theta)$ is a extremal point of the hyperellipse, n_{max} is bounded by (for more details see Appendix F):

$$n_{max} = \max\left(\min\left(n_{max}^{ari}, n_{max}^{geo}, n_{max}^{har}\right), n_{min} + 1\right) \tag{44}$$

Likewise, if $P_{min} = (0.5L_x + l_{min}, 0.5L_y + l_{min})$, n_{min} can be lower bounded by (see Appendix F):

$$n_{min} = \max\left(n_{min}^{ari}, n_{min}^{geo}, n_{min}^{har}, 2\right) \tag{45}$$

where the minimum value of 2 is considered because the admissible curve must not be a hypoellipse ($n < 2$) and remembering that the exponents considered in this work are integers. Moreover, the limits calculated by Eqs. 44 and 45 must still satisfy Eq. 42 so the left side in this equation must be less than or equal to 1. The terms $n_*^{ari}, n_*^{geo}, n_*^{har}$ are integer exponents based on arithmetic, geometric and harmonic means, respectively (see Appendix F for details), and they are defined as:

$$n_*^{ari} = \left\lceil \frac{\ln\left(\frac{1}{2}\right)}{\ln\left(\frac{x_*+y_*}{a+b}\right)} \right\rceil, \quad n_*^{geo} = \left\lceil \frac{\ln\left(\frac{1}{4}\right)}{\ln\left(\frac{x_*y_*}{ab}\right)} \right\rceil, \quad n_*^{har} = \left\lceil \frac{\ln\left(\frac{1}{2}\right)}{\ln\left(\frac{\frac{1}{a}+\frac{1}{b}}{\frac{1}{x_*}+\frac{1}{y_*}}\right)} \right\rceil \tag{46}$$

with $\lceil\cdot\rceil$ as the ceiling function, x_* and y_* as the point coordinates of P_{min} or P_{max} according to the case (Fig. 12), and a and b as the semi-axes of the hyperellipse (see Section 2.6 for their definitions). On the other hand, when the exponent n is selected the hyperelliptical layer is added to the original model and a remeshing process is necessary. Here, this process starts from a rectangular mesh with dimensions $2a \times 2b$ (its left bottom corner at the origin) with element size l_{min} and then elements crossed by the hyperelliptical border are deformed. The remaining elements outside it are discarded. Nodes belonging to crossed elements outside the curve will now be boundary nodes and they require to be relocated by using the parametric description of a hyperellipse[1] (see Fig. 13):

$$x = a|\cos r|^{\frac{2}{n}} \operatorname{sgn}(\cos r) \quad \text{and} \quad y = b|\sin r|^{\frac{2}{n}} \operatorname{sgn}(\sin r) \quad \therefore \quad 0 \le r \le 2\pi \tag{47}$$

where $\operatorname{sgn}(\cdot)$ is the sign function. Therefore, the new absolute coordinates $P_{new} = (x_{new}, y_{new})$ for a point with original coordinates $P_{ori} = (x_{ori}, y_{ori})$ and relative coordinates $P_{rel} = (x_{rel}, y_{rel}) = (x_{ori} - a, y_{ori} - b)$ outside the curve is:

$$x_{new} = a\left(1 + |\cos r|^{\frac{2}{n}} \operatorname{sgn}(\cos r)\right) \text{ and } y_{new} = b\left(1 + |\sin r|^{\frac{2}{n}} \operatorname{sgn}(\sin r)\right) \text{ and } r = \tan^{-1}\left(\frac{\operatorname{sgn}(y_{rel})\left|\frac{y_{rel}}{b}\right|^{\frac{n}{2}}}{\operatorname{sgn}(x_{rel})\left|\frac{x_{rel}}{a}\right|^{\frac{n}{2}}}\right) \tag{48}$$

This mapping must be done carefully, as it can lead to distorted elements in coarse meshes as n increases or in refined meshes as n decreases.

3.4. Implementation Flowchart

This work is done considering the wave vibration amplitude as the state variable. However, in areas such as Acoustics or Geology, the state variable may be pressure or density, being the pressure fluctuations easier to measure in reality than density, velocity, or displacement oscillations [87]. Therefore, the proposal here shown is applicable for any phenomenon governed by the scalar wave equation (Eq. 35) regardless of the type of state variable.

Figure 14 shows the flowchart for modeling with the proposed methodology for HABCs. First, a reference model and the required data for solving the problem are specified. The discretization parameters are defined by Eq. 39. In the reference model, the Eikonal equation in Eq. 41 is solved and the critical points are determined following the criterion explained in Section 2.5. At these points, the frequency response of the transient response in the reference model is computed via the Fast Fourier Transform (FFT), and the reference frequency f_{REF} (see Fig. 15), the propagation speed on the original boundary c_Γ and the distance L_s from the source are sought. Thus, the parameter $a_* = \frac{c_\Gamma}{f_{REF} L_s} \approx \frac{1}{f_{REF}\phi_{min}}$ in Eq. 9 can be determined (see Section 2.6).

Therefore, $f_{REF}(\phi_{min}) = f_{min}$ is the dominant frequency of the response at the point where ϕ_{min} is found (see Sections 2.5 and 3.2 for its calculation). However, the frequency of the response is unknown *a priori* and it can be assumed as the frequency of the excitation source, then initially $f_{REF} = f_s$. In a second step, $f_{REF} = f_{min}$ can be estimated via FFT and to correct the size of the AL (see Fig. 15). Nonetheless, in the inverse problem, this is not required since f_{REF} is updated according to FFT applied to response in the previous iteration. The candidate critical points are determined on the vertical and horizontal boundaries of bidimensional domains independently to evaluate the errors. Nevertheless, when the model have multiple sources (see Section 4.3), the point with minimum ϕ_{min} and the closest source (named as critical source) to this point determine the distance L_s for sizing the AL.

[1] Weisstein, E. W. "Superellipse". From MathWorld–A Wolfram Web Resource. https://mathworld.wolfram.com/Superellipse.html

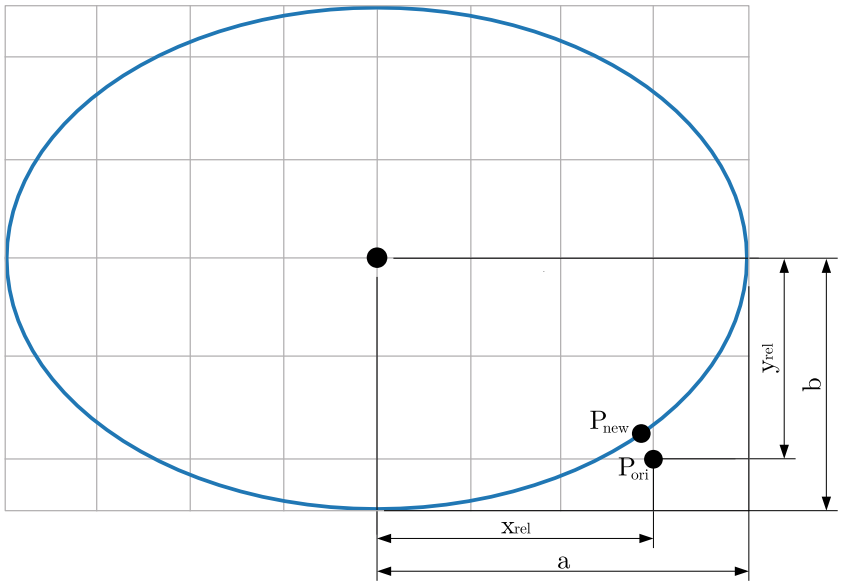

Fig. 13. Relocation of mesh nodes using the parametric description of a hyperellipse.

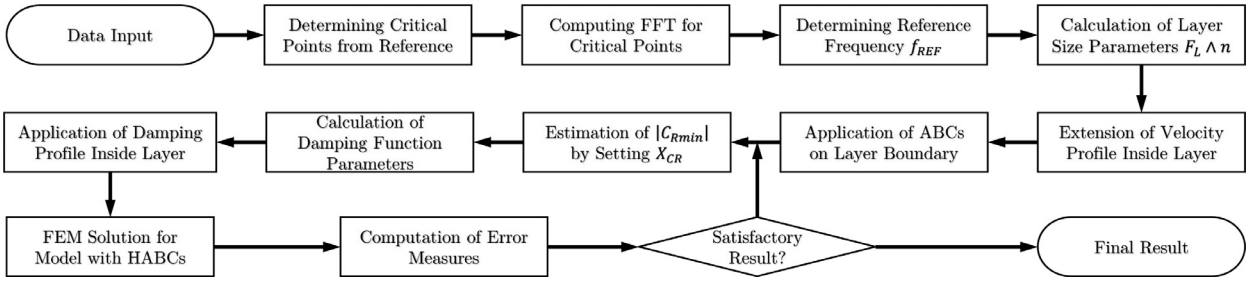

Fig. 14. Flowchart for modeling with proposed HABCs.

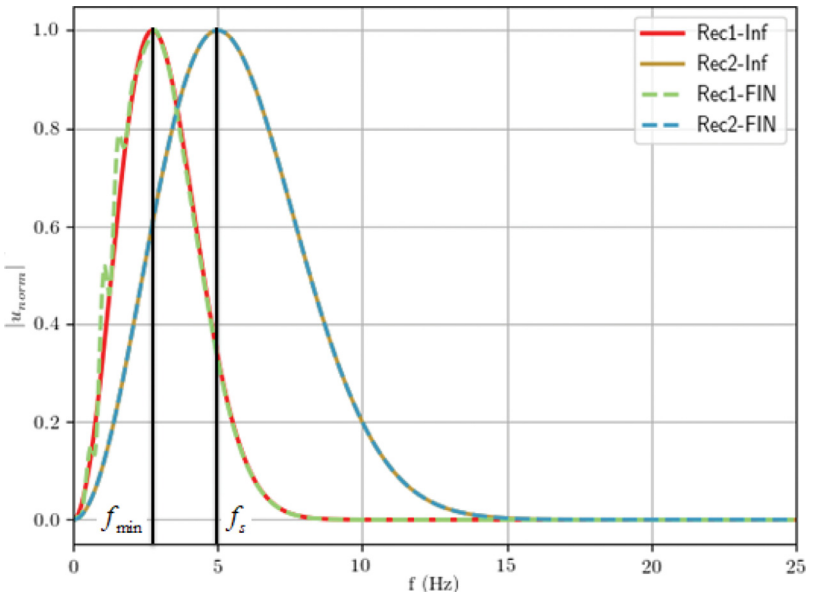

Fig. 15. Example of frequency response indicating f_s and $f_{\min}$.

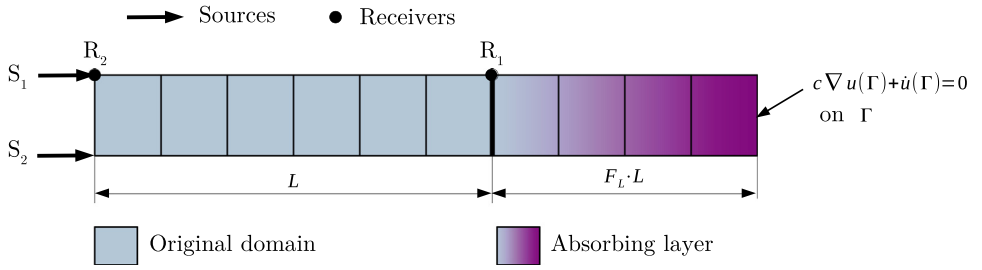

Fig. 16. Model for tests of AL in 1D.

The size parameter F_L is figured out by finding the first root of the Eq. 11 as explained in Section 2.3. Nevertheless, for bidimensional problems, since the reference distance L_s is usually less than any original domain dimension and the medium studied can be heterogeneous, the appropriate size for the problem may be an n-th root of this expression so that, the smallest possible size that meets the requirements is chosen. Besides, in bidimensional ones, the shape layer is selected between rectangular or hyperelliptical. It should be noted that the allowable integer exponents for the hyperelliptical layers are bounded by n_{min} and n_{max} (see Section 3.3 for their definitions).

The layer is added to the original model and the resulting one is remeshed as shown in Section 3.3. The velocity profile is extended for unidimensional models while for bidimensional ones, two strategies may be adopted: extension by straight continuity or by circular sectors (Fig. 10). Then, NRBCs are applied on the layer boundary (Eq. 34) and $|C_{Rmin}|$ is initially set to $X_{CR} = X^*_{CR}$ (see Eq. 25) or $X_{CR} = X^{ini}_{C_R}$ (Eq. 18) when $X^*_{C_R} < \xi_{max} d$. Next, the damping function is defined by calculating the parameters shown in Eq. 12 and the damping profile is applied within the AL. Remembering that damping is not considered neither in the original domain nor in the reference model.

The transient FEM problem governed by Eq. 36 is solved and the response is acquired at the critical points. After this simulation, the error measures are computed at these points, and the trapezoidal rule is used to calculate the integral terms of the integral error e_I with $N_{\Delta t}$ time steps (Eq. 31). The peak error e_P is determined by the maximum peaks observed in the response in the time interval $t \in [0, t_f]$ (Eq. 32). If the result is satisfactory, that is, the error measures tend to zero, the process is ended. Otherwise, the parameter $X^{min}_{C_R} \leq X_{C_R} \leq X^{max}_{C_R}$ (see definitions and limits from Eq. 27 to Eq. 29) is readjusted and the damping profile is modified for a new simulation until a minimum error value is reached. This fit follows a numerical line search process assuming that e_I is a unimodal function and taking a new search interval with half the length of the previous one when the error value starts to increase, as described by Arora [88].

Finally, in order to calculate the computational resources used, the execution time t_{exe} and the memory used M_{em} are measured. These parameters have been estimated for all the numerical results by using a PC architecture with an Intel Core i9-9900K Processor at 3.6GHz-16MB Cache 8 Cores-16 Threads, 64GB HyperX DDR4-2400MHz Kingston RAM, an SSD Drive Kingston SATA A400-480Gb SATA III for the operating system, an HD Drive Seagate BarraCuda SATA III-1Tb at 7200RPM for data storage and a PNY NVidia Quadro graphic card P5000 PCI Express-16GB 2560 CUDA Cores.

4. Numerical Results

Numerical examples presented here include a unidimensional model for the purposes of verification and validation of the methodology and two bidimensional models to show the potential and performance of the proposed approach. Besides, the results are compared with other strategies used traditionally.

4.1. Unidimensional Problem

Consider the problem in Fig. 16 whose objective is to calculate the AL size and damping parameters by using the methodology exposed in Sections 2.3 and 2.4. The source frequency is $f_s = 5\ Hz$ and the length of the original domain is a function of the central wavelength of the source λ_s, then $L = N_w \frac{c}{f_s}$. Positions of sources S_i and receivers R_i (points of evaluation of the response for this case) are shown in Fig 16.

The sources are unitary Ricker wave type and the receiver R_1 is located at the beginning of the AL (boundary of the original domain). The receiver R_2 is located at the position of the source S_1. The length of the homogeneous bar is $L = 4\lambda_s$ ($N_w = 4$) and $c = 1.5\ \frac{km}{s}$. The reference model (named **INF**) for error evaluation has a length of $L = 24\lambda_s$ and no damping or AL is considered. The final time considered in the simulation is $t_f = 4\ s$. Therefore, a comparative study is carried out considering two cases for the number of points (5 and 20) for representing the central wavelength of the source F_R (Eq. 39).

The number of time steps $N_{\Delta t}$ used for solving the transient FEM (Eq. 36) and the factor X_{C_R} used in QUA damping distributions (Eq. 16) are shown in Table 1. For unidimensional problems, X_{C_R} can be easily determined iteratively because of the computational cost is not an issue. However, for bidimensional ones (see numerical results in Sections 4.2 and 4.3), estimations for X_{CR} are extremely useful to aid in the selection of X_{CR} since the execution times of several models of this type can be prohibitive.

Table 1
Additional data for unidimensional models analyzed.

F_R	$N_{\Delta t}$	X_{CR} for QUA Damping	
		I Model	F Model
5	180	0.64	0.54
20	679	0.53	0.52

Table 2
Comparison of the results for $F_R = 5$.

Model Data		Damping Data			Layer Data			Error Results		Used Resources	
M	D	f(Hz)	ξ	$\eta_{max} \cdot 10^{-2}$	N_{el}	$\frac{L_\xi}{\lambda_{sou}}$	F_L	$e_I(\%)$	$e_P(\%)$	t_{exe}(s)	M_{em}(MB)
SOM		N/A					0.000	0.00	0.35	5.20	6.10
FSM	QUA	1.64	0.999	1.308	12	2.400	0.600	0.68	3.39	11.81	6.14
	OP2							0.84	2.26	15.44	6.10
	OP1							0.88	4.14	15.59	
	OP3							1.05	0.95	15.48	
	LSI							1.55	3.76	15.86	
ISM	OP3	5.03		3.923	4	0.800	0.200	8.21	11.10	7.53	6.05
	OP2							9.53	8.51	7.42	6.03
	QUA							10.26	4.57	9.38	6.07
	OP1							11.45	1.45	11.58	6.10
	LSI							13.58	8.65		6.03

Obs: Model(M), Damping(D).

Table 3
Comparison of the results for $F_R = 20$.

Model Data		Damping Data			Layer Data			Error Results		Used Resources	
M	D	f(Hz)	ξ	$\eta_{max} \cdot 10^{-2}$	N_{el}	$\frac{L_\xi}{\lambda_{sou}}$	F_L	$e_I(\%)$	$e_P(\%)$	t_{exe}(s)	M_{em}(MB)
SOM		N/A					0.000	0.00	0.06	11.94	6.24
FSM	QUA	2.75	0.999	2.242	28	1.400	0.350	0.91	3.55	16.03	6.26
	OP1							1.10	4.44	25.47	6.25
	OP2							1.27	2.26	25.39	
	OP3							1.73	0.89	25.72	
	LSI							2.18	3.75	17.83	
ISM	QUA	5.00		3.923	16	0.800	0.200	4.80	7.49	16.39	6.29
	OP1							5.22	6.46	23.75	6.28
	OP2							5.60	8.06	23.22	6.25
	OP3							5.93	6.01	23.25	
	LSI							8.47	11.75	17.34	6.19

Obs: Model(M), Damping(D).

The results for the comparative study in unidimensional models are presented in Tables 2 and 3 where a QUA damping (Eq. 16) presents the best results for all cases considered. The time response in receivers for $F_R = 20$ is exhibited in Fig 17. The models are identified in the tables in column M according to:

- **SOM**: Model with Sommerfeld BC on right boundary without AL.
- **ISM**: Initial model considering AL based on the dominant frequency at the source point (at R_2).
- **FSM**: Final model considering AL based on dominant frequency at R_1 with $f_{REF} = f_{min}$ as the reference frequency (see Section 3.4).

All frequency responses are calculated from the reference model INF via FFT. The suffix SM for models I and F represents a Sommerfeld BC applied on the right end. Several damping distribution functions (see Appendix D) are considered in column D:

- **QUA**: Quadratic function proposed in Section 2.4.
- **OPN**: Polynomial function of degree N considering linear (OP1), quadratic (OP2), and cubic (OP3) functions.

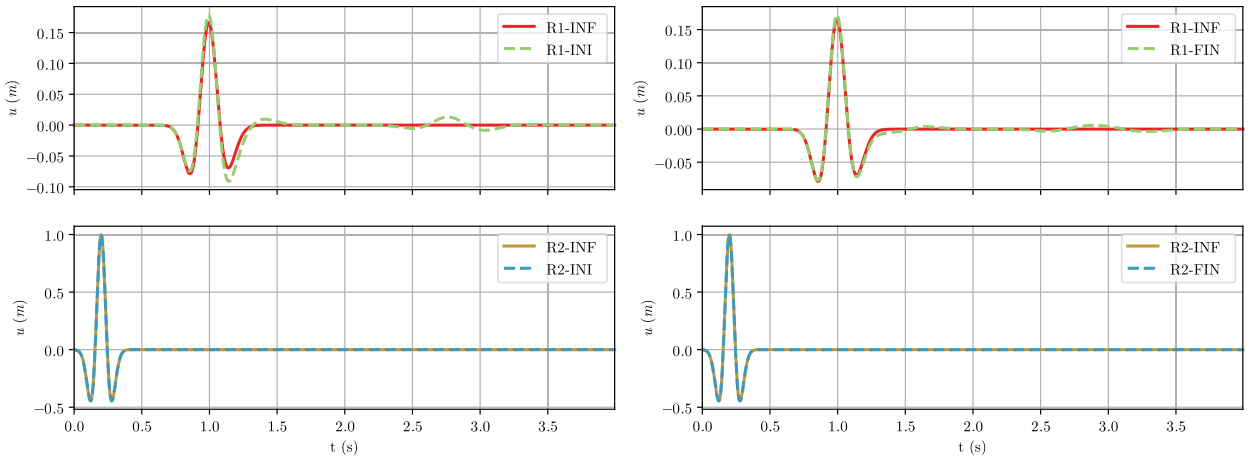

(a) Model ISM. (b) Model FSM.

Fig. 17. Time response in receivers for $F_R = 20$ and QUA damping distribution. *INF* in the legend is the reference signal.

- **LSI**: A combination between the OP1 distribution and a sinusoidal function [2] given by $\eta_{cr}\xi\left|x_i^{REF} - \frac{\sin 2\pi x_i^{REF}}{2\pi}\right|$.

The error measures are registered in the columns e_I and e_P Eqs. 31 and (32). The ratio $\frac{L_\xi}{\lambda_s}$ is the relation between the size of the AL $L_\xi = LF_L$ (Fig. 16) and the wavelength of the source. η_{max} is the maximum damping imposed inside the layer while N_{el} is the number of elements within the layer. The columns t_{exe} and M_{em} contain the execution time in seconds and the memory used in MB. The FSM-QUA models are highlighted in red color while the ISM-QUA ones are distinguished by blue color.

The results show that the dimensioned AL for the FSM models with QUA damping distribution is effective. Its errors are less than 1% for e_I and less than 4% for e_P. For the ISM models and the same damping function, the errors are less than 11% for e_I and less than 8% for e_P. The polynomial functions show errors less than 2% for e_I and less than 5% for e_P for the FSM models. While for the analogous ISM ones, the errors are less than 12% for both error measures. FSM-LSI models reach errors less than 3% for e_I and less than 4% for e_P. Nevertheless, the ISM-LSI one's present errors lower than 14% for e_I and less than 12% for e_P. However, the best results for all cases are presented by the FSM models with the proposed QUA damping distribution and the shortest execution times compared to the other FSM models. The used memory remains almost constant for all models considered.

On the other hand, the model SOM shows errors less than 1% for both error measures. Nevertheless, the use of an AL is justified to the detriment of computational cost for bidimensional models (see Sections 4.2 and 4.3). Here, the intention is to validate and verify the proposed methodology.

4.2. Bidimensional Problem

A bidimensional model is analysed to show the potential of the proposed HABCs. The original domain is a rectangle of dimensions $L_x = 2L_y$ being $L_x = N_w\frac{c_{min}}{f_s}$, with $N_w = 16$, $c_{min} = 1.5\ \frac{km}{s}$ and the source frequency $f_s = 5\ Hz$.

The source is the type Ricker with maximum amplitude 0.4 $\frac{kN}{kg}$ and it is located at $(0.35L_x, 0.75L_y)$ from the lower left corner of the original domain. Six receivers are distributed on its boundary and an additional receiver is located in the position of the source for a total of seven receivers (Fig. 18). The final time considered for the simulation is $t_f = 4s$. The tested layer shapes (Fig. 9) are rectangular (referred as **REC**) and hyperelliptical (referred as **EXX** where XX is the curve degree n, Eq. 33), satisfying the criteria presented in Section 3.3.

A comparative study is carried out on several types of models considering a small group of cases (Table 4) for the number of points representing the central wavelength of the source F_R (Eq. 39):

- **SOM**: Model with Sommerfeld BC on the original boundary without AL.
- **HIG**: Model with 1^{st}-Higdon BC on the original boundary without AL.
- **I|NRBC**: Initial model considering AL based on the dominant frequency at the source point (located at receiver R_7) with either Sommerfeld BC (**ISM**) or 1^{st}-Higdon BC (**IHG**).

[2] As implemented in Devito: Symbolic Finite Difference Computation, https://github.com/devitocodes/devito/blob/master/examples/seismic/abc_methods/02_damping.ipynb

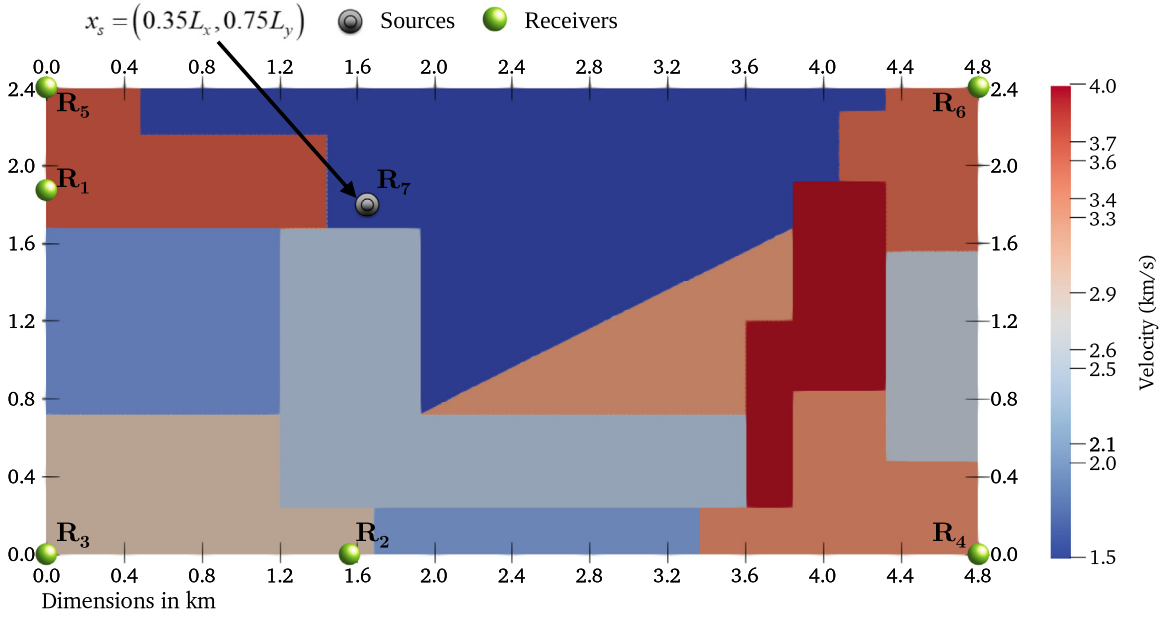

Fig. 18. Model for tests of HABCs in 2D.

Table 4
Additional data for bidimensional models analyzed.

F_R	l_{min} (m)	$N_{\Delta t}$	X_{CR}		I Models		F Models	
			L Extension	C Extension	n_{min}	n_{max}	n_{min}	n_{max}
8	37.50	1000	0.53	0.80	3	6	3	5
13	23.08	1640	0.23	0.45		5		
14	21.43	1760		0.39		6		
16	18.75	2000	0.27	0.51				

- **F|NRBC**: Final model considering AL based on dominant frequency at the critical point (receiver R_1) with $f_{REF} = f_{min}$ as the reference frequency. The NRBCs on the AL boundary may be either Sommerfeld (**FSM**) or 1^{st}-Higdon (**FHG**).

It should be remembered that the increase in the area due to the AL is quantified by the area factor F_A (see definition in Section 3). The damping distribution functions considered here are (see expressions in Appendix D):

- **QUA**: Quadratic function proposed in Section 2.4.
- **OPN**: Polynomial function of degree N with the original domain boundary as a reference. Linear (OP1), quadratic (OP2), and cubic (OP3) functions are considered.
- **LSI**: Function combining the OP1 distribution and a sinusoidal function [3] expressed as $\eta_{cr}\xi\left|x_i^{REF} - \frac{\sin 2\pi x_i^{REF}}{2\pi}\right|$.
- **RAD**: Radial with center at the original domain centroid.
- **ELL**: Elliptical with center at the original domain centroid.

The velocity profile extension can alternate between the two options shown in Section 2.6, either extension by straight continuity (suffix **L**) or by circular sectors (suffix **C**). The factor X_{C_R} used in QUA damping distributions and the minimum and maximum exponents (n_{min} and n_{max}, Eqs. 44 and 45) for hyperelliptical layers according to the model are shown in Table 4. In addition to the number of time steps $N_{\Delta t}$ used for solving the transient FEM (see Eq. 36) and the minimal dimension of the FE l_{min} (see Eq. 39). The numerical results for this comparative study are presented from Table 5 to Table 8.

The process for executing the set of models is the following: First, models with AL (I and F models) with only QUA damping distribution, for all the shapes considered (REC and EXX in Table 4) and all remaining options (extension strategies, NRBCs on the outer boundary), are executed. Second, the shape with the best performance in the previous stage is selected for a comparative study. This study consists in modeling that layer shape with other damping distributions (OP1, OP2, OP3, LSI, RAD, and ELL) for all models with AL (I and F models), extension strategies (L and C) and NRBCs on the outer boundary

[3] As implemented in Devito: Symbolic Finite Difference Computation, https://github.com/devitocodes/devito/blob/master/examples/seismic/abc_methods/02_damping.ipynb

Table 5
Comparison of the results for $F_R = 8$ and extension by straight continuity.

Model Data			Damping Data			Layer Data			Error Results		Used Resources	
M	S	D	f(Hz)	ξ	$\eta_{max} \cdot 10^{-3}$	N_{el}	$\frac{L_\xi}{\lambda_{sou}}$	F_A	e_I(%)	e_P(%)	t_{exe}(m)	M_{em}(MB)
FHG	E03	QUA	3.60	0.999	5.968	16	2.000	1.437	2.53	4.13	2.97	11.50
		OP1							2.70	5.17	3.47	
		OP2							2.71	4.39	3.48	
		LSI							2.98	2.82	3.45	
		OP3							3.01	5.61	3.49	11.48
IHG	REC		3.85		6.606	15	1.875	1.524	5.06	6.99	3.66	
		OP2							6.08	9.08	3.65	11.50
FHG		QUA	3.60		6.524	16	2.000	1.562	7.00	8.76	3.11	11.53
IHG	E03	RAD	3.85		6.056	15	1.875	1.401	7.28	20.63	3.40	11.48
FHG	REC	OP1	3.60		6.524	16	2.000	1.562	8.34	8.99	3.56	11.52
IHG		LSI	3.85		6.606	15	1.875	1.524	9.84	14.11	3.67	11.50
	E03	ELL			6.056			1.401	11.47	27.95	3.43	11.47
FSM	REC	RAD	3.60		6.524	16	2.000	1.562	11.99	13.78	3.57	11.51
HIG				N/A				1.000	12.26	37.46	1.81	10.98
SOM									15.14	35.32	1.82	10.96
FSM	REC	ELL	3.60	0.999	6.524	16	2.000	1.562	17.58	21.79	3.58	11.51

Obs: Model(M), Shape(S), Damping(D).

Table 6
Comparison of the results for $F_R = 8$ and extension by circular sectors.

Model Data			Damping Data			Layer Data			Error Results		Used Resources	
M	S	D	f(Hz)	ξ	$\eta_{max} \cdot 10^{-3}$	N_{el}	$\frac{L_\xi}{\lambda_{sou}}$	F_A	e_I(%)	e_P(%)	t_{exe}(m)	M_{em}(MB)
FHG	E03	QUA	3.60	0.999	5.968	16	2.000	1.437	3.49	4.30	3.00	11.50
		OP1							3.51	4.63	3.47	
		OP2							4.03	4.65	3.48	
		LSI							4.27	2.80	3.46	
FSM		OP3							4.43	4.24	3.49	11.47
IHG	REC		3.85		6.606	15	1.875	1.524	6.39	6.97	3.67	11.50
FHG		OP2	3.60		6.524	16	2.000	1.562	7.10	8.21	3.60	11.52
IHG	E03	RAD	3.85		6.056	15	1.875	1.401	7.60	20.00	3.40	11.48
FHG	REC	QUA	3.60		6.524	16	2.000	1.562	8.18	8.74	3.12	11.53
		OP1							8.69	8.85	3.58	11.52
IHG		LSI	3.85		6.606	15	1.875	1.524	10.58	13.89	3.66	11.50
	E03	ELL			6.056			1.401	11.50	27.08	3.46	11.48
FSM	REC	RAD	3.60		6.524	16	2.000	1.562	11.77	12.82	3.60	11.51
HIG				N/A				1.000	12.29	38.17	1.82	10.98
SOM									14.61	36.02		10.96
FSM	REC	ELL	3.60	0.999	6.524	16	2.000	1.562	17.28	20.57	3.60	11.51

Obs: Model(M), Shape(S), Damping(D).

(-SM and -HG). Finally, models without AL (SOM and HIG) are executed in order to complete the process. At most a total of 132 models are executed in this study for each value of F_R. Therefore, only the best result for rectangular and hyperellptical layers with each damping distribution are presented. Besides, the best EXX-QUA model is highlighted in red color while the REC-QUA one is distinguished by blue color. Likewise, the columns t_{exe} and M_{em} contain the execution time in minutes, and the memory used in MB, respectively. For the calculation of the ratio $\frac{L_\xi}{\lambda_s}$ in bidimensional cases, the size of the AL is $L_\xi = F_L L_s$. Due to space restrictions, only results for $F_R = 8$ and $F_R = 16$ are shown.

The models are identified as MOD-SHP-DMP, where MOD corresponds to the model with the NRBC applied on the corresponding boundary (SOM, HIG for models without layer, and ISM, IHG, FSM, and FHG for models with HABCs) and SHP for the layer shape (REC and EXX) while DMP represents the damping distribution (QUA, RAD, ELL or OPN). Eventually, if an E suffix is specified MOD-SHP-DMP-E, the model is identified by the extension strategy of the velocity profile. Then a

Table 7
Comparison of the results for $F_R = 16$ and extension by straight continuity.

Model Data			Damping Data			Layer Data			Error Results		Used Resources	
M	S	D	f(Hz)	ξ	$\eta_{max} \cdot 10^{-3}$	N_{el}	$\frac{L_\xi}{\lambda_{sou}}$	F_A	e_I(%)	e_P(%)	t_{exe}(m)	M_{em}(MB)
FHG	E03	QUA	3.60	0.999	6.112	33	2.063	1.455	2.97	6.27	29.79	14.95
		OP2							3.07	6.04	28.53	14.94
IHG		OP1	3.80		6.201	31	1.938	1.419	3.20	6.50	29.18	14.85
FHG		OP3	3.60		6.112	33	2.063	1.455	3.30	6.75	28.71	14.95
		LSI							3.37	4.12	29.05	14.92
	REC	OP3			6.687			1.582	5.33	6.76	34.05	15.16
		QUA							5.68	6.05	34.39	
		OP2							5.69	7.00	33.88	
		OP1							6.48	5.12	33.97	15.18
IHG	E03	RAD	3.80		6.201	31	1.938	1.419	8.06	22.30	28.92	14.87
FSM	REC		3.60		6.687	33	2.063	1.582	8.32	14.67	34.60	15.15
FHG		LSI							8.47	9.82	34.50	15.16
HIG				N/A				1.000	11.37	35.40	15.62	13.00
IHG	E03	ELL	3.80	0.999	6.201	31	1.938	1.419	12.15	27.98	29.20	14.85
FSM	REC		3.60		6.687	33	2.063	1.582	12.82	21.27	34.11	15.12
SOM				N/A				1.000	18.23	38.49	15.74	12.96

Obs: Model(M), Shape(S), Damping(D).

Table 8
Comparison of the results for $F_R = 16$ and extension by circular sectors.

Model Data			Damping Data			Layer Data			Error Results		Used Resources	
M	S	D	f(Hz)	ξ	$\eta_{max} \cdot 10^{-3}$	N_{el}	$\frac{L_\xi}{\lambda_{sou}}$	F_A	e_I(%)	e_P(%)	t_{exe}(m)	M_{em}(MB)
FHG	E03	QUA	3.60	0.999	6.112	33	2.063	1.455	4.37	7.75	25.75	14.93
IHG		OP1	3.80		6.201	31	1.938	1.419	4.51	6.78	29.26	14.85
		OP2	3.60		6.112	33	2.063	1.455	4.66	7.78	28.63	14.95
		OP3							4.94	8.94	28.68	
FHG		LSI							5.09	5.10	28.47	14.92
	REC	QUA			6.687			1.582	6.98	5.93	33.71	15.14
		OP3							7.14	7.04	34.03	15.16
		OP2							7.21	7.58	33.84	
FSM		OP1							7.22	7.45	34.04	15.13
		RAD							8.68	13.90	34.47	
IHG	E03		3.80		6.201	31	1.938	1.419	8.93	21.85	29.07	14.85
FHG	REC	LSI	3.60		6.687	33	2.063	1.582	9.77	10.40	34.44	15.14
HIG				N/A				1.000	11.46	35.91	15.59	13.00
IHG	E03	ELL	3.80	0.999	6.201	31	1.938	1.419	12.90	27.22	29.13	14.85
FSM	REC		3.60		6.687	33	2.063	1.582	13.28	20.08	34.12	15.13
SOM				N/A				1.000	17.54	36.97	15.66	12.96

Obs: Model(M), Shape(S), Damping(D).

model FHG-E03-QUA-C is the identifier for the model considering AL based on the dominant frequency $f_{REF}(\phi_{min}) = f_{min}$ and a 1^{st}-Higdon BC on its boundary with hyperelliptical layer of the degree $n = 3$, and quadratic damping distribution as explained in Section 2.4. The label C at the end of the identifier represents an extension of the velocity profile by circular sectors (Fig. 10).

Best results for all cases are achieved by the hyperelliptical layers with QUA damping distribution inside them combined with a 1^{st}-Higdon BC on the boundary layer. The layer is determined based on the dominant frequency at the corresponding critical point. Nonetheless, some I models are present in the best results, *i.e.*, models considering AL based on the dominant frequency at the source point. In this case, the dominant frequency at this point does not correspond to the central frequency of the source because it is close to the boundaries of other regions with different propagation speed (Fig. 18). Thus,

Table 9
Summary of the results for proposed QUA damping distribution.

Model	Damping Data			Layer Data			Error Results		Used Resources	
	f_{REF}(Hz)	X_{CR}	$\eta_{max} \cdot 10^{-3}$	N_{el}	$\frac{L_\xi}{\lambda_{sou}}$	F_A	e_I(%)	e_P(%)	t_{exe}(m)	M_{em}(MB)
Hyperelliptical Layers (EXX) with Extension by Straight Continuity (L)										
FHG-E03-F_R08	3.60	0.53	5.968	16	2.000	1.437	2.53	4.13	2.97	11.50
FHG-E03-F_R13		0.23	6.071	27	2.077	1.459	3.04	7.50	13.63	13.53
FHG-E03-F_R14			6.156	29	2.071	1.457	3.22	5.35	18.03	13.97
FHG-E03-F_R16		0.27	6.112	33	2.063	1.455	2.97	6.27	29.79	14.95
Hyperelliptical Layers (EXX) with Extension by Circular Sectors (C)										
FHG-E03-F_R08	3.60	0.83	5.968	16	2.000	1.437	3.49	4.30	3.00	11.50
FHG-E03-F_R13		0.45	6.071	27	2.077	1.459	4.41	9.17	13.63	13.51
FHG-E03-F_R14		0.39	6.156	29	2.071	1.457	4.59	6.90	18.00	13.98
FHG-E03-F_R16		0.51	6.112	33	2.063	1.455	4.37	7.75	25.75	14.93
Rectangular Layers (REC) with Extension by Straight Continuity (L)										
FHG-F_R08	3.60	0.53	6.524	16	2.000	1.562	7.00	8.76	3.11	11.53
FHG-F_R13		0.23	6.645	27	2.077	1.587	6.14	7.46	15.11	13.65
FHG-F_R14			6.737	29	2.071	1.585	5.71	7.69	24.28	14.15
FHG-F_R16		0.27	6.687	33	2.063	1.582	5.68	6.05	34.39	15.16
Rectangular Layers (REC) with Extension by Circular Sectors (C)										
FHG-F_R08	3.60	0.83	6.524	16	2.000	1.562	8.18	8.74	3.12	11.53
FHG-F_R13		0.45	6.645	27	2.077	1.587	7.48	5.90	15.14	13.66
FHG-F_R14		0.39	6.737	29	2.071	1.585	6.95	6.70	24.33	14.15
FHG-F_R16		0.51	6.687	33	2.063	1.582	6.98	5.93	33.71	15.14

when the excitation wave hits these boundaries originates reflections that produce constructive or destructive interference with the source wave and the dominant frequency is different from the source frequency.

On the other hand, hyperelliptical layers of degree $n = 4$ for cases such as $F_R = 14$ with extension by circular sectors and $F_R = 16$ with extension by straight continuity failed due to the mesh modification, as the elements can be distorted by large variations. Nevertheless, in hyperelliptical layers with higher degrees as $n = 5$ or $n = 6$, the elements can be distorted despite the little movement of the nodes causing the mode not to run. This situation is presented for $n = 5$ and $F_R = 8$ for both strategies of extension of the velocity and, for $n = 6$ and both $F_R = 14$ and $F_R = 16$ with extension by straight continuity. Other strategies for the meshing of these irregular domains may be implemented in order to circumvent this issue.

The model with only Sommerfeld BC shows errors between 3.7 and 6.1 times for e_I and between 3.8 and 9 times for e_P compared to the values for the best result at each case. The errors for the model with only 1st-Higdon BC are between 2.4 and 4.8 times for e_I and between 4 and 9.2 times for e_P relative to the same reference values. Therefore, the use of an AL is justified to the detriment of computational cost. However, there is a trade-off between the magnitude of the error and the amount of material added to the original model since a very large F_L can entail a high cost of computational resources. Nevertheless, the area increment factor F_A is between 1.437 and 1.459 for hyperelliptical layers, and between 1.562 and 1.587 for rectangular ones.

The summary of the results for the proposed QUA damping distribution are shown in Table 9. The models in column M are identified according to the explained previously, and it is added a suffix F_RXX for the number of points used for representing the central wavelength of the source λ_{sou}. The hyperelliptical layers of $n = 3$ for models F-F_R16 and the time response in receivers for model FHG-E03-QUA-F_R16 considering the different extension strategies are exhibited in Fig. 19 and Fig. 20, respectively. Observing Tab. 9, it is noticeable that, for both types of extension of the profile velocity inside the layer, hyperelliptical layers show errors less than 4.6% and 9.2% for e_I and e_P, respectively; rectangular ones present errors less than 8.2% and 8.8% for e_I and e_P, in that order; keeping in mind that all models use a 1st-Higdon BC. No relevant results are reported for models with Sommerfeld BC and hyperlliptical layers of degree greater than 3.

Still in Tab. 9, the hyperelliptical layers show a computational cost reduction between 3.8% and 26.1%; and less than 1.4% memory usage savings. Now, comparing the performance between analogous layers with different extensions, rectangular layers with extension by straight continuity show lower error measures in all cases. In turn, the same behavior is observed in hyperelliptical layers with extension by straight continuity compared to analogous ones with extension by circular sectors. The differences in error measures for extension strategies are between 37% and 48% for hyperelliptical layers and 16% and 23% for rectangular layers, and discrepancies of less than 0.2% in memory usage. Moreover, the factor X_{C_R} in the models with extension by circular sectors is greater than in models with extension by straight continuity in ratios between 56% and 96%. It should be noted that the results are affected by the rounding up of the size of the AL derived from the size of the finite element (see Eq. 40). Thus, the best performance in the analyzed cases is achieved using hyperelliptical layers with

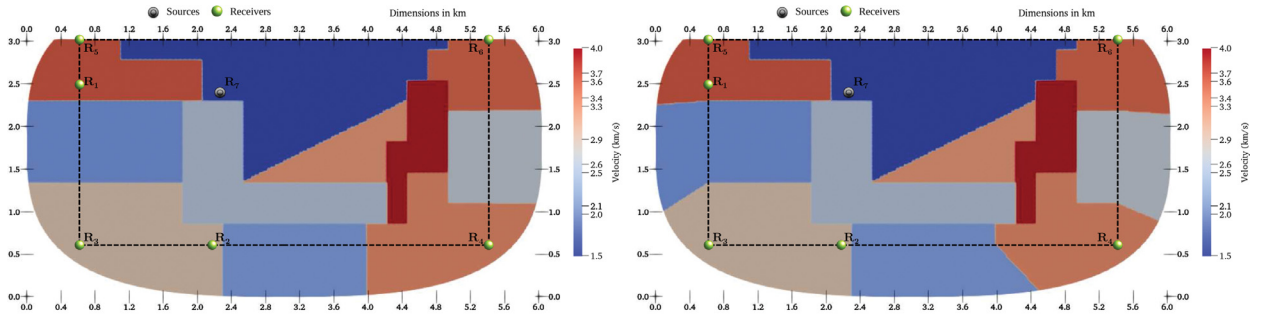

(a) Extension by straight continuity (L). (b) Extension by circular sectors (C).

Fig. 19. Distribution of the speed propagation in models F-E03-F_R16. The dotted line on the plots is the domain of interest.

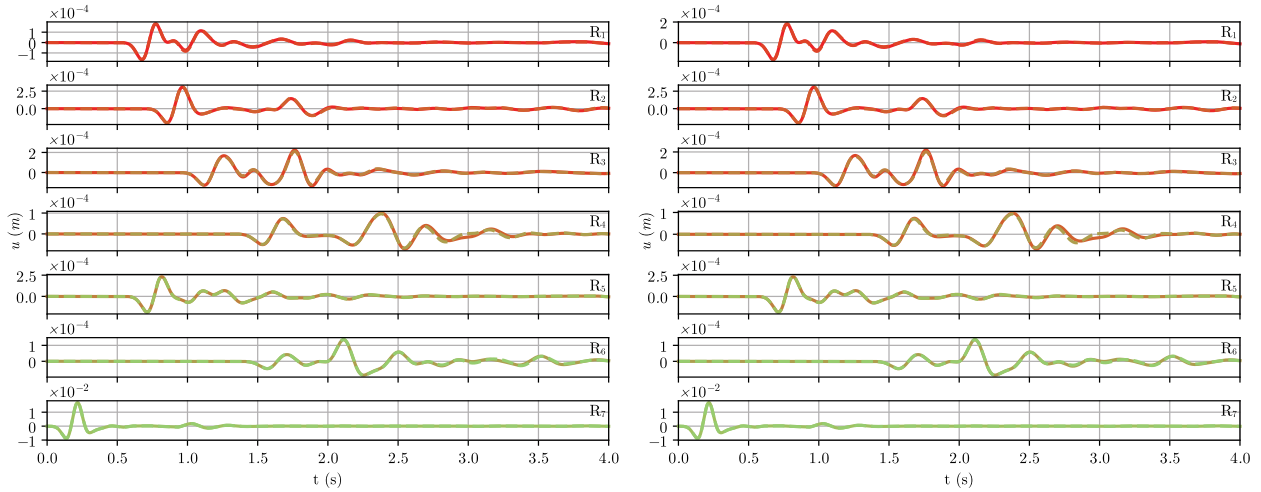

(a) Extension by straight continuity (L). (b) Extension by circular sectors (C).

Fig. 20. Time response in receivers for model FHG-E03-QUA-F_R16. The solid line on the plots is the reference signal.

extension by straight continuity, given that the errors and execution time are the lowest. On the other hand, rectangular layers have the highest errors independent of the type of extension.

4.3. Marmousi Model

Marmousi Model was created in the *Institut Francais du Pétrole* (IFP) in 1988 [82]. This data set is considered a benchmark for geophysical purposes. The model version considered in this work was downloaded to https://sites.google.com/a/kaust.edu.sa/tariq/research/anismarmousi whose dimensions are $9.2km\ x\ 3km$ (see Fig. 21) and the mesh consists of $736\ x\ 240$ finite elements with $l_{min} = 12.5m$. The minimum propagation speed is $c_{min} = 1.5\frac{km}{s}$ while the maximum is $c_{max} = 5.5\frac{km}{s}$. The sources are unitary Ricker with central frequency $f_s = 6\ Hz$ and located as shown in Fig. 21 (sources depth: $25m$).

Nevertheless, the AL size is determined by the closest source to the point on the original boundary with the lowest arrival time ϕ_{min}, naming it as the critical source (Fig. 21). Again, six receivers are distributed on its boundary and an additional receiver is located in the position of the critical source for a total of seven receivers. Thus, R_1 is the point identified by the lowest arrival time ϕ_{min} of the entire model, R_2 is the point with the lowest arrival time on vertical boundaries and R_7 is the point of the critical source. Likewise, the reference distance L_s is the distance from R_7 to R_1. Since the data set has a fixed mesh size, the number of time steps Δt is governed by the number of points representing the central wavelength of the source F_R (see Eq. 39). Therefore, $F_R = 20$ is selected for this problem and the final time considered for the simulation is $t_f = 3.5\ s$. Consequently, the number of time steps used for solving the transient FEM (Eq. 36) is $N_{\Delta t} = 3422$.

Model types, layer shapes, damping distribution functions, velocity profile extensions, and, the nomenclature used are the same as the problem in Section 4.2. Data additional for the problem is shown Table 10, including the heuristic factor X_{C_R} used in QUA damping distributions (Eq. 16). Final models, or F models, are only considered in this study. That is, those in which AL size is based on the reference frequency $f_{REF} = f_{min}$ at the corresponding critical point.

This example shows that the appropriate size for the layer may not be the first root of Eq. 11, different from the model studied in Section 4.2. Although the reference distance L_s is almost the domain height, the medium has a high heterogeneity

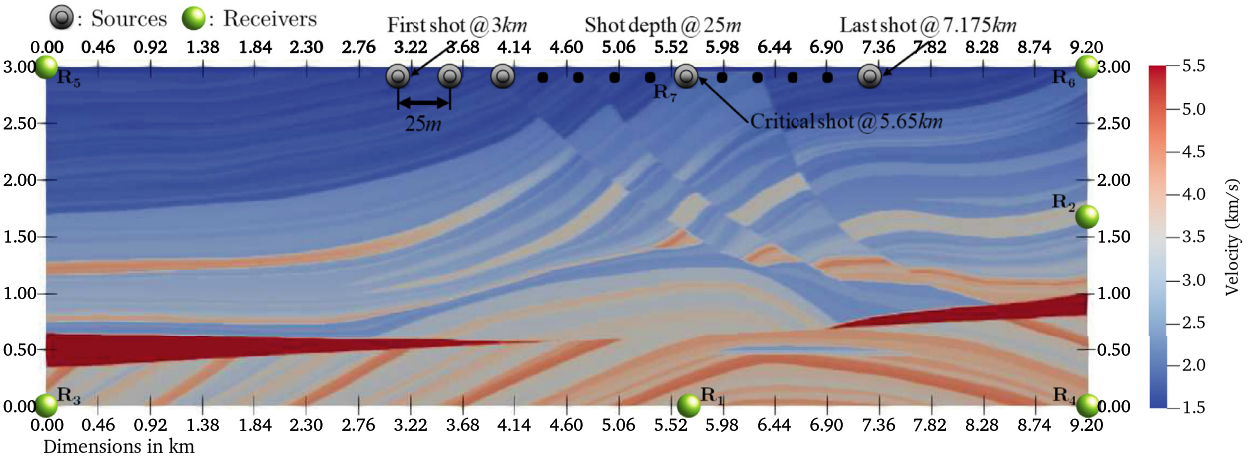

Fig. 21. Marmousi Model for tests of HABCs in 2D.

Table 10
Additional data for Marmousi model analysis.

F_R	l_{min} (m)	$N_{\Delta t}$	f_{REF}(Hz)	X_{CR}		F_L	F Models	
				L Extension	C Extension		n_{min}	n_{max}
20	12.50	3422	3.37	1.99		0.2227	4	5
						0.3067	3	4
						0.3403		
						0.4748	2	3

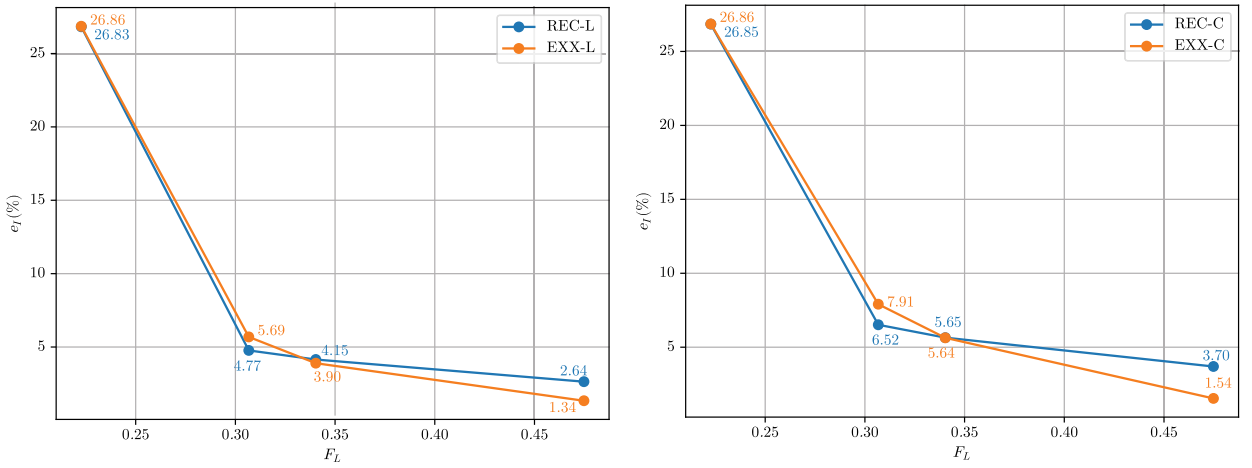

(a) Extension by straight continuity (L).

(b) Extension by circular sectors (C).

Fig. 22. Integral error e_I vs size parameter F_L for models FHG-QUA.

in the propagation speed profile. Here, a requirement for finding the proper layer size is to limit the integral error $e_I \leq 5\%$ after obtaining a greater one with the smallest size corresponding to the first root of Eq. 11. Thus, process for sizing layer is the following: First, F models with QUA damping distribution, for all the shapes considered (REC and EXX in Table 10) and all remaining options (extension strategies, NRBCs on the outer boundary), are executed for the smallest F_L (first root). If the integral error $e_I \leq 5\%$ for both extension strategies (L and C) the process finishes, otherwise the next size parameter F_L ($n+1$-th root in Eq. 11) is tested under the same conditions. It should be highlighted that, the criterion of Eq. 42 establishes different limits for the exponents (n_{min} and n_{max}) for the different cases of F_L (see Table 10).

Finally, the shape with the best performance for the last F_L tested in the previous stage is selected for a comparative study as done in Section 4.2 with analogous F models. Due to the large number of models considered in this study, only the best result for rectangular and hyperellptical layers with each damping distribution are presented. Again, models without AL (SOM and HIG) are executed in order to complete the comparison, and in the result tables, the best EXX-QUA model is

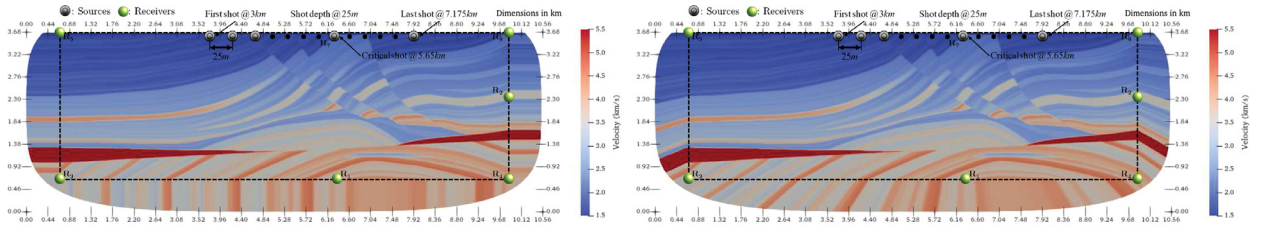

(a) Extension by straight continuity (L). (b) Extension by circular sectors (C).

Fig. 23. Distribution of the speed propagation in models FHG-E04 and $F_L = 0.2227$. The dotted line on the plots is the domain of interest.

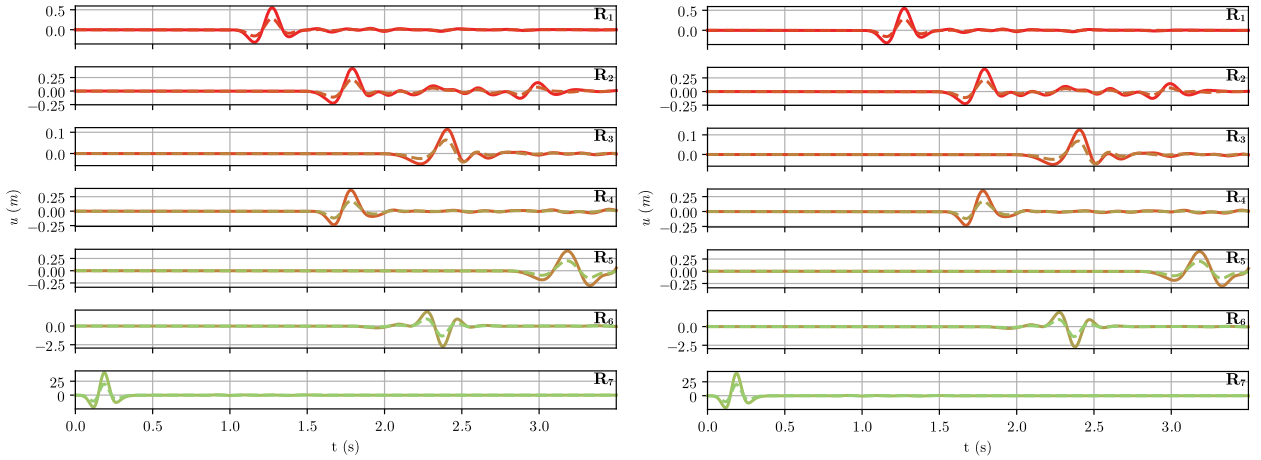

(a) Extension by straight continuity (L). (b) Extension by circular sectors (C).

Fig. 24. Time response in receivers for model FHG-E04-QUA and $F_L = 0.2227$. The solid line on the plots is the reference signal.

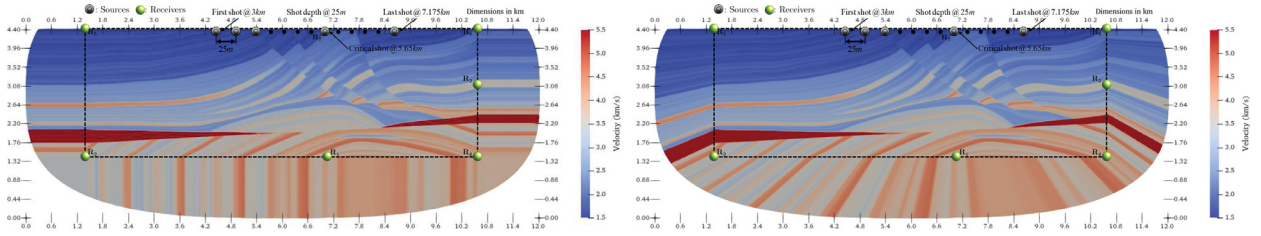

(a) Extension by straight continuity. (b) Extension by circular sectors.

Fig. 25. Distribution of the speed propagation in models FHG-E03 and $F_L = 0.4748$. The dotted line on the plots is the domain of interest.

highlighted in red color while the REC-QUA one is distinguished by blue color. In addition, the execution time t_{exe} for the models is reported in hours.

Figure 22 shows the lowest error obtained for rectangular and hyperelliptical layers for each case of F_L and the different extension strategies for the propagation speed within the layer, all models using a 1^{st}-Higdon BC. It should be noted that, the lowest errors in hyperelliptical layers are obtained with the exponent n_{min}, except for the case $F_L = 0.4748$, they are achieved with $n_{max} = 3$ (see Table 10). This can be attributed to the short distance between the domain corners and the layer border when $n = 2$.

For the first $F_L = 0.2227$, the lowest errors have practically no difference but they are greater than 26% even though the difference in the areas of the models is 4.8%. For the second $F_L = 0.3067$, rectangular layers outperform the hyperelliptical ones with 16.2% and 17.6% smaller errors for the L extension and for the C extension, respectively. On the contrary, for the remaining two cases of F_L, the hyperelliptical layers obtain the lowest error compared to the rectangular ones. For $F_L = 0.3403$, the error in hyperelliptical layers are 6.0% and 0.2% smaller errors for the L extension and for the C extension, respectively. While for $F_L = 0.4748$, the errors are smaller by 49.2% and 58.4% considering the same sequence. For these three last F_L the area difference is around 8%. However, the saving in computational cost for the hyperelliptical layers is between 12% and 21% while the reduction in memory usage can be up to 8%. The hyperelliptical layers with the lowest error for

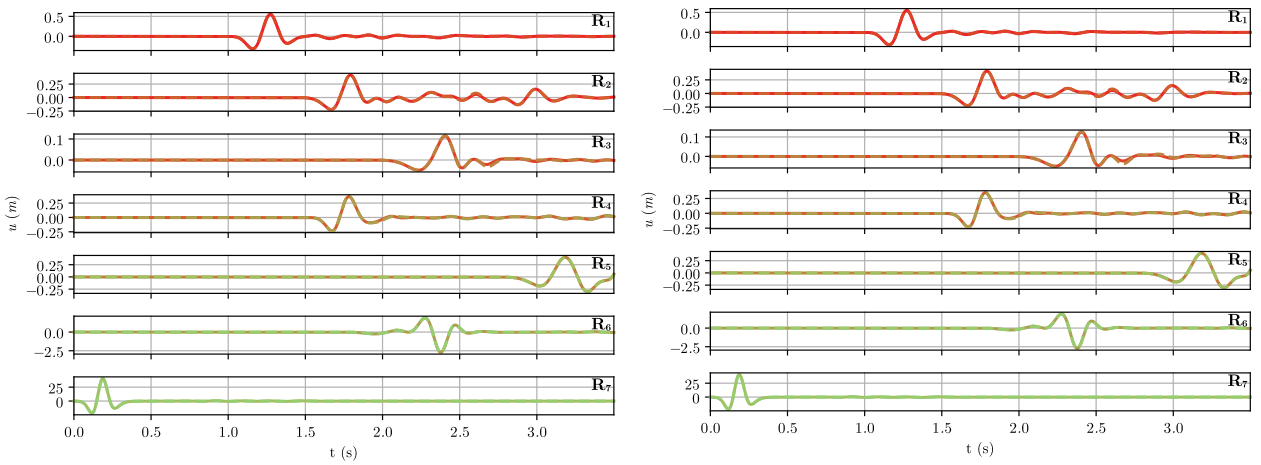

(a) Extension by straight continuity (L).

(b) Extension by circular sectors (C).

Fig. 26. Time response in receivers for model FHG-E03-QUA and $F_L = 0.4748$. The solid line on the plots is the reference signal.

Table 11
Comparison of the results for 1st-Higdon BC and extension by straight continuity.

Model Data			Damping Data			Layer Data			Error Results		Used Resources	
M	S	D	f(Hz)	ξ	$\eta_{max} \cdot 10^{-4}$	N_{el}	$\frac{L_\xi}{\lambda_{sou}}$	F_A	e_I(%)	e_P(%)	t_{exe}(h)	M_{em}(MB)
FHG	E03	QUA	3.37	0.999	4.177	113	5.650	1.767	1.34	1.66	3.01	24.20
		OP1							1.41	1.33	3.47	
		RAD							1.48	2.17		
		LSI							1.49	1.98		
		ELL							1.54	2.50	3.46	
		OP2							1.57	0.98		
		OP3							1.67	0.53		
	REC	QUA			4.040			1.922	2.64	1.63	3.77	26.22
		ELL							2.72	2.40	4.25	
		LSI							2.93	1.94	4.30	
		OP1							2.95	1.31	4.22	
		RAD							3.04	2.08	4.31	
		OP2							3.37	0.97	4.29	
		OP3							3.62	0.54		
HIG			N/A					1.000	42.13	47.84	1.55	16.20
SOM									81.76	76.64	1.56	16.19

Obs: Model(M), Shape(S), Damping(D).

$F_L = 0.2227$ and $F_L = 0.4748$ are displayed Fig. 23 and Fig. 25, respectively. Likewise, the time response in receivers for the same cases are exhibited Fig. 24 and Fig. 26, in that order.

The numerical results of the comparative study executed are presented in Table 11 and Table 12. Newly, the best results for all extension strategies are obtained by the hyperelliptical layers with QUA damping distribution inside them combined with a 1st-Higdon BC on the boundary layer. The errors for the model with only 1st-Higdon BC are 30.1 (C extension) and 31.4 (L extension) times for e_I and 28.8 (L extension) and 39.5 (C extension) times for e_P, relative to the values for the best result at each case. Similarly, the model with only Sommerfeld BC shows errors 54.9 (C extension) and 61 (L extension) times for e_I and 46.2 (L extension) and 59.2 (C extension) times for e_P, compared to the same reference values. Consequently, the computational cost increase between 1.9 and 2 times, and the memory usage of 1.5 times are justified by the use of an AL. On the other hand, the area increment factor F_A is 1.767 for hyperelliptical layers and 1.922 for rectangular ones.

Hyperelliptical layers obtain the best performances compared to rectangular layers for both cases of extension of the profile velocity inside the layer. The best results for hyperelliptical layers and 1st-Higdon BC show performances less than 1.6% for e_I and 1.7% for e_P while the rectangular ones present performances less than 3.7% for e_I and 1.7% for e_P, all models with the proposed QUA damping distribution. Besides, they show the lowest values in relation to computational cost and memory usage. As a consequence, hyperelliptical layers show a computational cost reduction between 19% and 20%, and around 7.8% memory usage savings. On the other hand, when contrasting analogous layers with different extension strategies, hyperellip-

Table 12
Comparison of the results for 1st-Higdon BC and extension by circular sectors.

Model Data			Damping Data			Layer Data			Error Results		Used Resources	
M	S	D	f(Hz)	ξ	$\eta_{max} \cdot 10^{-4}$	N_{el}	$\frac{L_\xi}{\lambda_{sou}}$	F_A	e_I(%)	e_P(%)	t_{exe}(h)	M_{em}(MB)
FHG	E03	QUA	3.37	0.999	4.177	113	5.650	1.767	1.54	1.33	3.02	24.20
		OP1							1.62	1.19	3.47	
		LSI							1.76	2.03	3.46	
		RAD								2.35	3.47	
		OP2							1.81	1.05		
		ELL							1.83	2.93	3.48	
		OP3							1.90	0.65	3.46	
		QUA							3.70	1.27	3.76	26.23
		ELL							3.79	2.85	4.26	26.22
		LSI							4.04	1.94	4.31	
	REC	OP1			4.040			1.922	4.12	1.13	4.28	
		RAD							4.51	2.30	4.30	
		OP2							4.66	0.98		
		OP3							4.99	0.59	4.28	
HIG				N/A				1.000	46.30	52.57	1.54	16.20
SOM									84.55	78.76	1.56	16.19

Obs: Model(M), Shape(S), Damping(D).

tical layers with extension by straight continuity show e_I between 12% and 16% lower than those with extension by circular sectors. The same fact is observed in rectangular ones whose e_I are smaller in a range between 27% and 33%. Likewise, the discrepancies are less than 0.6% in execution time and less than 1.4% in memory usage. By last, models with Sommerfeld BC reports errors greater than 11% for e_I and 0.5% for e_P considering both extension strategies of the propagation speed. In addition, they present analogous behaviors concerned with execution times and memory use.

5. Conclusions

A HABC scheme based on hyperelliptical ALs and an NRBC applied on its outer boundary is proposed. This methodology provides a unified criterion between the attenuation of the wave amplitude and the reflection coefficient at the beginning of the layer with the aiming of sizing properly an AL according to the problem. The proposed methodology is also applicable to both complete and partial layers, that is, with some of their boundaries acting as a free surface represented by a Neumann BC.

The critical point that controls the layer size is determined by means of the Eikonal analysis. Several sizes can be provided for this criterion, allowing to test different options and bound the maximum error desired, especially in highly heterogeneous media and models with sources far away from some original boundaries. In addition, an adaptive quadratic damping profile is formulated so that the maximum damping is given by an asymptotic limit for underdamped vibration and the minimum damping is selected with a criterion based on the reflection coefficient at the interface between the original domain and the AL. This approach to bound the damping is opposite to the typical ones found in the literature where the maximum damping is selected.

Hyperelliptical layers achieve better results than rectangular ones when the proposed quadratic damping profile is set up inside the layer. Moreover, the prescription of NRBCs increases the effectiveness of the layer, obtaining better results with the 1st-Higdon BC. Another important aspect to highlight is the implementation of two strategies for the extension of the propagation speed profile within the layer. Previous works do not address or recommend any methodology to follow for the extension of the profile. Here, two strategies are implemented: extension by straight continuity using the original truncated domain boundary as a reference and extension by circular sectors with respect to the source position. The former strategy shows lower error measures than the latter in hyperelliptical layers.

The optimized HABCs strategy proves efficient and promising as the damping parameters are selected by the proposed methodology and not by the user's expertise. This methodology deals with the absorbing phenomenon as a combination of the local dissipation (due to the progressive increase of the damping coefficient from an element to another) and global dispersion (due to the global effect of slowing down of the wave propagation speed and the consequent increase in the wave number) inside the absorbing layer and an NRBC on the boundary. Besides, the vibration regime inside the absorbing layer must be underdamped in order to avoid slowing down the system. The maximum damping parameter can be seen as a numerical property of the model since the portion of material added as an AL determines the limit damping for the underdamped regime.

From a computational point of view, hyperelliptical layers can reduce up to more than 20% and save up to 8% in memory usage related to rectangular ones according to the problem. However, no significant differences are found when comparing the ALs using the different strategies of propagation speed profiles. Furthermore, analytical approaches are proposed for saving computational effort such as the approximation of the fundamental frequency by using the results of the Eikonal analysis and geometric relationships. Nevertheless, the use of an approach with AL is justified due to the poor performance of the models with only NRBCs even though the computational cost is increased. The trade-off between the magnitude of the error and the amount of material added to the original model can be achieved by the different options provided by the sizing criterion.

In future works, an adaptive strategy for HABCs will be integrated into 2D and 3D inverse problems. It is expected that the HABCs selected for the forward problem are also suitable for the adjoint problem and the spurious signal acquired by the receivers is reduced with the aim of improving the robustness of the inversion algorithms.

Data Availability

Data will be made available on request.

Acknowledgements

We gratefully acknowledge support of the RCGI - Research Centre for Gas Innovation, hosted by the University of São Paulo (USP) and sponsored by FAPESP - São Paulo Research Foundation (2014/50279-4) and Shell Brasil, and the strategic importance of the support given by ANP (Brazil's National Oil, Natural Gas and Biofuels Agency) through the RD levy regulation. Moreover, the second author thank FAPESP (São Paulo Research Foundation) for his doctoral fellowship with number 2020/07557-4. The fourth author (E.C.N. Silva) is pleased to acknowledge the support by CNPq (National Council for Scientific and Technological Development) under grant 302658/2018-1.

Appendix A. Comparison of Natural Frequencies Between Free-Free and Free-Sommerfeld BC Bars

A comparison of the first 10 natural frequencies between a free-free bar and a free-Sommerfeld BC is performed by using COMSOL Multiphysics (Fig A.27) in order to estimate the difference in the free vibration regime.

Here, $L = 4.8\,km$ and $c = 1.5\,\frac{km}{s}$. These differences are less than 0.02% (Table A.1), so it can be concluded that the frequencies can be estimated without computational effort through the behavior of the free-free bar.

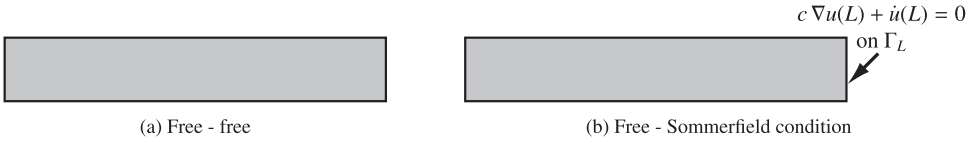

Fig. A27. Models for comparison of their first 10 natural frequencies.

Table A.1
Comparison of natural frequencies (in Hz) for free-free bar and free-Sommerfeld bar.

Modes	1	2	3	4	5	6	7	8	9	10
Free-Free	0.1563	0.3125	0.4688	0.6250	0.7813	0.9375	10.938	12.500	14.063	15.625
Free-Somm	0.1562		0.4687	0.6249	0.7811	0.9374		12.498	14.061	15.623
Difference	0.019%	0.016%	0.006%	0.018%	0.018%	0.016%	0.018%	0.016%	0.014%	0.013%

Appendix B. Formulation Details

The expressions for the dispersion relation, the wave number k and the loss factor l are [72]:

$$\text{Dispersion Relation} : \omega^2 - j\,\omega\,\eta = c^2\gamma^2,\ \gamma = k - j\,l$$

$$\text{Wave Number} : k = \sqrt{\frac{1}{2}\left(\frac{\omega}{c}\right)^2\left[1+\sqrt{1+\left(\frac{\eta}{\omega}\right)^2}\right]} \quad \text{and} \quad \text{Loss Factor} : l = \frac{\eta}{c\sqrt{2\left[1+\sqrt{1+\left(\frac{\eta}{\omega}\right)^2}\right]}} \tag{B.1}$$

remembering that k and l are found solving the system of equations by separating the real and imaginary parts of the dispersion relation. Thus, the expression for the speed propagation:

$$v_p = \frac{\omega}{k} = \frac{\sqrt{2}c}{\sqrt{1+\sqrt{1+\left(\frac{\eta}{\omega}\right)^2}}} \tag{B.2}$$

By using the approximation $(1+x)^{\frac{1}{2}} \approx 1+\frac{x}{2}$ for x small [89], the approximated speed propagation is:

$$v_p \approx \frac{c}{1+\frac{1}{8}\left(\frac{\eta}{\omega}\right)^2} \tag{B.3}$$

then, by substituting $\eta = 2\xi\omega_m$ and $\omega = 2\pi f$, the expression in Eq. 7 is obtained. Now, Eq. 8 is the parameterization of the unidimensional underdamped solution in relation to the amplitude attenuation factor R evaluated in $x = L_a$ at $t = t_a = \frac{L_a}{v_p}$ under the initial amplitude u_o, and depending on F_L. Remembering that L_a is the AL length, t_a is the instant time when the wave reaches the end of it for the first time and $F_L = \frac{L_a}{L}$ is the domain fraction that must be added as an AL (L is the length of the original domain). The underdamped solution is [90]:

$$u(t,x) = u_0 \exp\left(-\frac{\eta t}{2}\right)\left(\cos(\omega_d t) + \frac{\eta}{2\omega_d}\sin(\omega_d t)\right)\cos(k_a x) \tag{B.4}$$

with $\omega_d = \omega_m\sqrt{1-\xi^2}$ and $k_a = \frac{\omega}{v_p}$ as the damped frequency and the wave number, respectively. Likewise, $\omega = 2\pi f$ and $\omega_m = \frac{m\pi c}{L_a}$ are the angular wave frequency and the natural frequency of the AL, in that order. Thus:

$$\begin{aligned} R &= \left|\frac{u(t_a,L_a)}{u_0}\right| = \left|\exp\left(-\frac{\eta t_a}{2}\right)\left(\cos(\omega_d t_a) + \frac{\eta}{2\omega_d}\sin(\omega_d t_a)\right)\cos(k_a L_a)\right| \\ \frac{\eta t_a}{2} &= \xi m\pi A \quad , \ \omega_d t_a = m\pi A\sqrt{1-\xi^2} \text{ and } k_a L_a = \frac{2\pi F_L}{a_*}A \text{ with } A = 1+\frac{1}{2}\left(\frac{\xi m a_*}{2F_L}\right)^2 \text{ and } a_* = \frac{c}{fL} \end{aligned} \tag{B.5}$$

The substitution of the terms $\frac{\eta t_a}{2}$, $\omega_d t_a$ and $k_a L_a$ in R gives rise to the expression of Eq. 9. On the other hand, the magnitude of the reflection coefficient between two media taking into account the dispersion relation is [70]:

$$|C_R| = \left|\frac{k_1-k_2}{k_1+k_2}\right| = \left|\frac{v_{p2}-v_{p1}}{v_{p2}+v_{p1}}\right| = \left|\frac{\eta_2^2-\eta_1^2}{(4\omega)^2+\eta_2^2+\eta_1^2}\right| = \left|\frac{\xi_2^2-\xi_1^2}{\left(\frac{4F_L}{ma_*}\right)^2+\xi_2^2+\xi_1^2}\right| \tag{B.6}$$

However, $\xi_1 = 0$ at the interface between the original domain and the AL. Therefore, considering the above, the expression for the magnitude of the minimum reflection coefficient in Eq. 10 is achieved.

Appendix C. Regression for Determining the Factor $X^*_{C_R}$

The minimum damping ratio ξ_{min} in Eq. 16 is parameterized according to the number of elements by $\xi_{min} = X_{C_R} d$, being the term $X^{min}_{C_R} \le X_{C_R} \le X^{max}_{C_R}$ a heuristic factor determined by the user and $d = \frac{1}{N_{el}}$ (see Section 2.4). However, there is a value for X_{C_R} that maximizes the AL performance (see Section 2.5 for error measure definition). This factor $X^*_{C_R}$ can be approximated by the vertex of a convex parabola given by the quadratic equation:

$$|C_{Rmin}| = a_{C_R}X^2_{C_R} + b_{C_R}X_{C_R} + c_{C_R} \tag{C.1}$$

that can be defined by exactly three points. These points are $\left(X^{ini}_{C_R}, \left|C^{ini}_{Rmin}\right|\right)$, $\left(X^{max}_{C_R}, \left|C^{max}_{Rmin}\right|\right)$ and $\left(X^{\text{FEM}}_{C_R}, \left|C^{\text{FEM}}_{Rmin}\right|\right)$ and they are determined from the analysis performed in Section 2.4. Therefore, a system of three equations and three unknowns can be solved in order to compute the coefficients a_{C_R}, b_{C_R} and c_{C_R}, so that:

$$\begin{aligned} a_{C_R} &= \frac{m_2-m_1}{X^{\text{FEM}}_{C_R}-X^{max}_{C_R}} \\ b_{C_R} &= m_2 - a_{C_R}\left(X^{\text{FEM}}_{C_R}+X^{ini}_{C_R}\right) \\ c_{C_R} &= \left|C^{\text{FEM}}_{Rmin}\right| - X^{\text{FEM}}_{C_R}\left(m_2 - a_{C_R}X^{ini}_{C_R}\right) \\ \text{with } m_1 &= \frac{\left|C^{max}_{Rmin}\right| - \left|C^{ini}_{Rmin}\right|}{X^{max}_{C_R}-X^{ini}_{C_R}} \text{ and } m_2 = \frac{\left|C^{\text{FEM}}_{Rmin}\right| - \left|C^{ini}_{Rmin}\right|}{X^{\text{FEM}}_{C_R}-X^{ini}_{C_R}} \end{aligned} \tag{C.2}$$

then, the vertex of the Eq. C.1 sets up the desired value for X_{C_R} and is given by:

$$X^*_{C_R} = -\frac{b_{C_R}}{2a_{C_R}} = \frac{m_2\left(X^{max}_{C_R} + X^{ini}_{C_R}\right) - m_1\left(X^{\mathrm{FEM}}_{C_R} + X^{ini}_{C_R}\right)}{2(m_2 - m_1)} \tag{C.3}$$

However, since it must be satisfied $X_{C_R} \geq \xi_{max} d$, $X^*_{C_R}$ is substituted for $X^{ini}_{C_R}$ when $X_{C_R} < \xi_{max} d$ (see Section 2.4).

Appendix D. Equivalent Factor $X^{\mathrm{RDF}}_{C_R}$ for Different Damping Distribution Functions

Since the value X_{C_R} is unknown *a priori* (only its extremal values are known), reference values to start its search can be determined by equaling the expressions for $|C_{Rmin}|$ of the proposed quadratic damping distribution (Eq. 16) and a known function *RDF* acting as a reference (see Section 2.4). The reference damping functions depending on the position used in this work are:

- **Polynomial Function of Degree N (OPN)**:

$$\nu^{OPN}_{\xi}\left(x^{REF}_i\right) = \xi_{max}\left(x^{REF}_i\right)^N \tag{D.1}$$

- **Linear Combined with Sine Function (LSI)** [4]:

$$\nu^{LSI}_{\xi}\left(x^{REF}_i\right) = \xi_{max}\left|x^{REF}_i - \frac{\sin 2\pi x^{REF}_i}{2\pi}\right| \tag{D.2}$$

- **Radial Function (RAD)**:

$$\nu^{RAD}_{\xi}(x_i) = \xi_{max}\sum_i \left(\frac{x_i}{0.5L_{\max} + L_{\xi}}\right)^2 \therefore L_{\max} = \max(L_x, L_y) \tag{D.3}$$

- **Elliptical Function (ELL)**:

$$\nu^{ELL}_{\xi}(x_i) = \xi_{max}\sum_i \left(\frac{x_i}{0.5L_i + L_{\xi}}\right)^2 \therefore L_i = L_x, L_y \tag{D.4}$$

with x^{REF}_i as the reference distance based on the original domain boundary (Fig. 7), x_i as the reference distance based on the original domain centroid and remembering that $\xi_{max} = 0.999$. The equivalent factor $X^{\mathrm{RDF}}_{C_R}$ is obtained solving the equality $\left|C^{\mathrm{QUA}}_{Rmin}\right| = \left|C^{\mathrm{RDF}}_{Rmin}\right|$, that is:

$$\left|\frac{(X_{C_R} d)^2}{\left(\frac{4F_L}{ma_*}\right)^2 + (X_{C_R} d)^2}\right| = \left|\frac{\left(\nu^{RDF}_{\xi}\left(x^*_i\right)\right)^2}{\left(\frac{4F_L}{ma_*}\right)^2 + \left(\nu^{RDF}_{\xi}\left(x^*_i\right)\right)^2}\right| \tag{D.5}$$

where the reference damping function is evaluated at the node closest to the border of the original domain with relative coordinates x^*_i (see from Eq. D.1 to Eq. D.4). Thus, solving Eq. D.5 for X_{C_R} is obtained:

- **Polynomial Function of Degree N (OPN)**:

$$X^{OPN}_{C_R} = \xi_{max} d^{N-1} \therefore x^*_i = d \tag{D.6}$$

- **Linear Combined with Sine Function (LSI)**:

$$X^{LSI}_{C_R} = \xi_{max}\left|1 - \frac{\sin 2\pi d}{2\pi d}\right| \therefore x^*_i = d \tag{D.7}$$

- **Radial Function (RAD)**:

$$X^{RAD}_{C_R} = \frac{\xi_{max}}{d}\left(\frac{0.5L_{\min} + l_{min}}{0.5L_{\max} + L_{\xi}}\right)^2 \therefore x^*_i = 0.5L_{\min} + l_{min} \wedge L_{\min} = \min(L_x, L_y) \wedge L_{\max} = \max(L_x, L_y) \tag{D.8}$$

[4] As implemented in Devito: Symbolic Finite Difference Computation, https://github.com/devitocodes/devito/blob/master/examples/seismic/abc_methods/02_damping.ipynb

- **Elliptical Function (ELL)**:

$$X_{C_R}^{ELL} = \frac{\xi_{max}}{d} \min\left(\left[\frac{0.5L_i + l_{min}}{0.5L_i + L_\xi}\right]^2\right) \therefore x_i^* = 0.5L_i + l_{min} \wedge L_i = L_x, L_y \tag{D.9}$$

being l_{min} defined in Eq. 39. Here, RAD and ELL functions are only used in bidimensional problems.

Appendix E. Analytical Calculation of the Fundamental Frequency

The fundamental frequency of a rectangular domain ($2a \times 2b$) with homogeneous speed propagation c is [5]:

$$\omega_{1R} = \frac{\pi c}{2}\sqrt{\frac{1}{a^2} + \frac{1}{b^2}} = cF_{\omega_R} \quad \therefore \quad F_{\omega_R} = \frac{\pi}{2}\sqrt{\frac{1}{a^2} + \frac{1}{b^2}} \tag{E.1}$$

while that of an elliptical domain (hyperellipse of degree $n = 2$) with semi-axes a and b is [78,83]:

$$\omega_{1E} = \frac{2}{f_E} c\sqrt{M_{01}} = cF_{\omega_E} \quad f_E = \sqrt{a^2 - b^2} \quad \therefore \quad F_{\omega_E} = \frac{2}{f_E}\sqrt{M_{01}} \tag{E.2}$$

where M_{01} is the first root of the zero-order modified Mathieu's function evaluated at special input paremeter $\xi_0 = \operatorname{arccosh}\left(\frac{a}{f_E}\right)$. Here, it is determined iteratively in Python.[6]

The fundamental frequency of a hyperelliptical domain increases in relation to the decrease in area. Thus, it is reasonable that the fundamental frequency can be estimated by a function depending on the area and bounded by elliptical ($n = 2$) and rectangular ($n = \infty$) frequency factors F_{ω_E} and F_{ω_R}. The area of a hyperellipse of degree n with semi-axes a and b is given by the expression [7]:

$$A_H = 4ab\frac{\left(\Gamma\left(1 + \frac{1}{2}\right)\right)^2}{\Gamma\left(1 + \frac{2}{n}\right)} = abF_{A_H} \quad \therefore \quad F_{A_H} = 4\frac{\left(\Gamma\left(1 + \frac{1}{2}\right)\right)^2}{\Gamma\left(1 + \frac{2}{n}\right)} \tag{E.3}$$

with $\Gamma(\cdot)$ as the Gamma function and, F_{A_H} as a hyperelliptical area factor depending on the degree n. Therefore, $F_{A_H} = \pi$, $A_H = \pi ab$ for an ellipse ($n = 2$), and $F_{A_H} = 4$, $A_H = A_R = 4ab$ for a rectangle ($n = \infty$) with dimensions $2a \times 2b$. The area of a partial hyperelliptical geometry as considered in Section 2.6 can be determined as [8]:

$$A_{Hp} = \frac{abF_{A_H}}{2} + 2a\sum_{r=0}^{\infty}\binom{\frac{1}{n}}{r}\frac{(-1)^r y^{nr+1}}{b^{nr}(nr+1)} \tag{E.4}$$

being the term $\binom{\frac{1}{n}}{r}$ the r-th binomial coefficient. Table E.1 shows the factor F_{A_H} for different values of n and a percentage difference $\Delta A_R(\%) = 1 - \frac{A_H}{A_R}$ in relation to the area of a rectangle.

[5] García, A. F. "Modos de Vibración de una Membrana Rectangular". From Curso Interactivo de Física en Internet. http://www.sc.ehu.es/sbweb/fisica3/ondas/membrana_1/membrana_1.html

[6] Scipy implementation in Python: mathieu_modcem1($m = 0,\ q = M_{01},\ x = \xi_0$). https://docs.scipy.org/doc/scipy/reference/generated/scipy.special.mathieu_modcem1.html\#scipy.special.mathieu_modcem1.

[7] Weisstein, E. W. "Superellipse". From MathWorld–A Wolfram Web Resource. https://mathworld.wolfram.com/Superellipse.html.

[8] "Superellipse (Lame curve)". From Alien's Mathematics. https://fractional-calculus.com/super_ellipse.pdf.

Table E1
Area factor F_{A_H} for different degrees n.

n	F_{A_H}	$\Delta A_R(\%)$
2	π	21.46
3	3.533278	11.67
4	3.708149	7.30
5	3.800601	4.99
6	3.855243	3.62
7	3.890175	2.75
8	3.913843	2.15
9	3.930614	1.74
10	3.942928	1.43
20	3.984695	0.38
50	3.997444	0.06
∞	4	0

By observing Eqs. E.1 and E.2, the fundamental frequency ω_{1H} of a hyperellipse of degree $n > 2$ can be calculated analogously, considering a frequency factor depending on semi-axes and the curve degree:

$$\omega_{1H} = cF_{\omega_H}(a, b, n) \tag{E.5}$$

In addition, approximations of the fundamental frequencies of hyperellipses can be made with a certain degree of uncertainty by restricting their search to frequencies of similar known geometries of equal or comparable area [84].

Thus, it is acceptable consider ω_{1H} between ω_{1R} and ω_{1E} and consequently $F_{\omega_R} \leq F_{\omega_H} \leq F_{\omega_E}$. When a complete hyperelliptical layer of degree $n \geq 3$ or a partial one with $n \geq 2$ are added to the original model, the limits for F_{ω_H} are defined by:

$$\frac{\pi}{2}\sqrt{\frac{1}{a^2}+\frac{1}{b^2}} = F_{\omega_R} \leq F_{\omega_H} \leq F_{\omega_E} = 2\sqrt{\frac{M_{01}}{a^2-b^2}} \tag{E.6}$$

Therefore, the proposed function for frequency factor F_{ω_H} is:

$$F_{\omega_H} = F_{\omega_R}\left(1-(1-R_F)\left(\frac{2}{n}\right)^p\right) \quad \text{with} \quad p = 1.694535 \quad \text{and} \quad R_F = \frac{F_{\omega_E}}{F_{\omega_R}} \tag{E.7}$$

where the term R_F ensures that the computed frequency is between ω_R and ω_E and p is obtained making a regression of F_{A_H} vs n considering the proposed model $F_{A_H} = 4\left(1-\left(1-\frac{\pi}{4}\right)\left(\frac{n}{2}\right)^p\right)$ (Table E.1). That is, the factor F_{A_H} in Eq. E.3 can be approximated by this expression without using the Gamma function.

Finally, the fundamental frequency of a hyperellipse with homogeneous material properties can be approximately calculated as:

$$\omega_{1H} = cF_{\omega_H} \tag{E.8}$$

On the other hand, ω_1 can be estimated in heterogeneous media based on the minimum arrival time ϕ_{min} in the reference model. If Eq. 30 is applied to a unidimensional domain (Fig. 3) without considering the pseudo-viscosity μ_{eik}, it can be seen as:

$$|\nabla\phi| = \left|\frac{\mathrm{d}\phi}{\mathrm{d}x}\right| \approx \frac{\Delta\phi}{\Delta x} \approx \frac{\phi-\phi_s}{x-x_s} = \frac{1}{c} \tag{E.9}$$

where the subscript s refers to the values evaluated at wave source position. As seen in Sections 2.5 and 3.2, for the evaluation of ϕ as the arrival time at each point of the domain, $\phi_s = 0$. Now, if the wave source is located at a tip and $\phi = \phi_\Gamma$ is evaluated at the other end (on the boundary) then $L = x - x_s$. Thus, taking into account that $\omega_1 = \frac{\pi c}{L}$ (see Appendix B):

$$\omega_1 = \frac{1}{k_\omega \phi} \;\therefore\; \frac{c}{L} = \frac{1}{\phi} \tag{E.10}$$

then $k_\omega = \frac{1}{\pi}$ for the unidimensional case with homogeneous propagation speed c. Likewise, for heterogeneous media, a factor k_ω is proposed according to the domain dimensions, so that:

$$k_\omega = F_{\omega\mathrm{REF}} L_s = \frac{\pi L_s}{2a}\sqrt{1+R_A^2} \tag{E.11}$$

with $F_{\omega\mathrm{REF}}$ obtained from Eq. E.1 considering the dimensions and the aspect ratio $R_A = \frac{a}{b}$ of the original rectangular domain. Remembering that, L_s is the distance from the source to the point belonging to the original boundary where ϕ_{min} is found. Hence, the approximated fundamental frequency in the reference model $\omega_{1\mathrm{REF}}$ (original model without AL) is:

$$\omega_{1\mathrm{REF}} = \frac{1}{k_\omega \phi_{min}} \tag{E.12}$$

with k_ω computed from Eq. E.11 and ϕ_{min} obtained from solution of Eq. 41. By analysing Eq. E.12, assuming that $\frac{c_{eq}}{L_s} = \frac{1}{\phi_{min}}$ and comparing to Eq. E.1, the reference frequency can be seen:

$$\omega_{1\mathrm{REF}} = c_{eq}\, F_{\omega\mathrm{REF}} F_{\mathrm{GHM}} \quad \therefore \quad F_{\omega\mathrm{HM}} = \left(\frac{1}{1+R_A^2}\right)\left(\frac{2a}{\pi L_s}\right)^2 \tag{E.13}$$

with c_{eq} as an equivalent propagation speed inferred from the eikonal solution and F_{GHM} as a fictitious correction factor by geometry for heterogeneous media. Nonetheless, more accurate values for $\omega_{1\mathrm{REF}}$ according to the discretization can be sought via modal analysis, with a corresponding increase in the computational cost. Consequently, the fundamental frequency for a model with AL can be approximated as:

$$\omega_1 = \omega_{1\mathrm{REF}} \frac{F_{\omega*}}{F_{\omega\mathrm{REF}}} \tag{E.14}$$

being the factor $F_{\omega*}$ calculated according to the layer shape (see Eqs. E.1, E.2 or E.7). It should be noted, $F_{\omega*} < F_{\omega\mathrm{REF}}$ since the area of the model with AL is smaller.

Appendix F. Determining the Limits for Hyperelliptical Exponents

The extremal points ("corners") in a hyperellipse of degree n centered at the origin and semi-axes a and b are defined by the parameter named *superness* represented by s [85,86]. The extremal points are given by the coordinates $(\pm sa, \pm sb)$. Therefore, substituting these values in Eq. 33:

$$2|s|^n = 1 \Rightarrow s = \pm 2^{-(1/n)} \therefore |x_{max}| = sa \wedge |y_{max}| = sb \tag{F.1}$$

and the parameter r in Eq. 47 is $r = \frac{\pi}{4}$, remembering that this parameter is not the angle in standard position. If the coordinates of an extremal point are (x_*, y_*), the coordinates can be parameterized relative to the *superness* and the degree of the hyperellipse, so that:

$$x_* = \frac{a}{2^{(1/n_*)}}, \quad \text{and} \quad y_* = \frac{b}{2^{(1/n_*)}} \tag{F.2}$$

which constitutes an equation system with more equations than unknowns but that must be satisfied simultaneously. The only unknown variable is n, since a, b, x_* and y_* are defined when the layer size parameters are determined (see Sections 2.6 and 3.3). Thus, a measure of central tendency can help in solving this problem so that the arithmetic, geometric and harmonic mean are considered here. They are defined as [91,92]:

$$\bar{x}_{ari} = \frac{1}{N}\sum_{i=1}^{N} x_i, \quad \bar{x}_{geo} = \left(\prod_{i=1}^{N} x_i\right)^{\frac{1}{N}}, \quad \bar{x}_{har} = N\left(\sum_{i=1}^{N} \frac{1}{x_i}\right)^{-1} \tag{F.3}$$

Therefore, the measures of central tendency are applied, obtaining for each case:

$$x_* + y_* = 2^{(-1/n_*^{ari})}(a+b), \quad x_* y_* = 2^{(-2/n_*^{geo})}(ab), \quad \frac{1}{x_*} + \frac{1}{y_*} = 2^{(1/n_*^{har})}\left(\frac{1}{a} + \frac{1}{b}\right) \tag{F.4}$$

then solving for n_*^{ari}, n_*^{geo} and n_*^{har} and taking into account that these terms are integer numbers, the expressions in Eq. 46 are found.

References

[1] D. Givoli, Computational Absorbing Boundaries, in: S. Marburg, B. Nolte (Eds.), Computational Acoustics of Noise Propagation in Fluids -Finite and Boundary Element Methods, Springer-Verlag, Berlin, 2008, pp. 145–166, doi:10.1007/978-3-540-77448-8.

[2] S.V. Tsynkov, Numerical solution of problems on unbounded domains. A review, Applied Numerical Mathematics 27 (4) (1998) 465–532, doi:10.1016/S0168-9274(98)00025-7.

[3] J.-P. Bérenger, A historical review of the absorbing boundary conditions for electromagnetics, Forum for Electromagnetic Research Methods and Application Technologies 9 (6) (2015) 1–28.

[4] G.C. Cohen, High-Order Numerical Methods for Trasient Wave Equations, 1st, Springer-Verlag Berlin Heidelberg, New York, 2002, doi:10.1007/978-3-662-04823-8.

[5] D. Givoli, High-order local non-reflecting boundary conditions: A review, Wave Motion 39 (4) (2004) 319–326, doi:10.1016/j.wavemoti.2003.12.004.

[6] Y. Gao, H. Song, J. Zhang, Z. Yao, Comparison of artificial absorbing boundaries for acoustic wave equation modelling, Exploration Geophysics 48 (1) (2017) 76–93, doi:10.1071/EG15068.

[7] F. Pled, C. Desceliers, Review and recent developments on the Perfectly Matched Layer (PML) method for the numerical modeling and simulation of elastic wave propagation in unbounded domains, Archives of Computational Methods in Engineering 29 (1) (2022) 471–518, doi:10.1007/s11831-021-09581-y.

[8] H. Espinoza, R. Codina, S. Badia, A Sommerfeld non-reflecting boundary condition for the wave equation in mixed form, Computer Methods in Applied Mechanics and Engineering 276 (2014) 122–148, doi:10.1016/j.cma.2014.03.015.

[9] P. Wellens, M. Borsboom, A generating and absorbing boundary condition for dispersive waves in detailed simulations of free-surface flow interaction with marine structures, Computers and Fluids 200 (2020) 1–13, doi:10.1016/j.compfluid.2019.104387.

[10] J.A. Lorenzzetti, J.D. Wang, On the use of wave-absorbing layers in the treatment of open boundaries in numerical coastal circulation models, Applied Mathematical Modelling 10 (5) (1986) 339–345, doi:10.1016/0307-904X(86)90093-4.

[11] R. Holland, J.W. Williams, Total-field versus scatttered-field finite-difference codes: A comparative assessment, IEEE Transactions on Nuclear Science 30 (6) (1983) 4583–4588, doi:10.1109/TNS.1983.4333175.

[12] J.-P. Bérenger, A perfectly matched layer for the absorption of electromagnetic waves, Journal of Computational Physics 114 (2) (1994) 185–200, doi:10.1006/jcph.1994.1159.

[13] E. Turkel, A. Yefet, Absorbing PML boundary layers for wave-like equations, Applied Numerical Mathematics 27 (4) (1998) 533–557, doi:10.1016/S0168-9274(98)00026-9.

[14] C. Cerjan, D. Kosloff, R. Kosloff, M. Reshef, A nonreflecting boundary condition for discrete acoustic and elastic wave equations, Geophysics 50 (4) (1985) 705–708, doi:10.1190/1.1441945.

[15] W.A. Mulder, Experiments with Higdon's absorbing boundary conditions for a number of wave equations, Computational Geosciences 1 (1997) 85–108, doi:10.1023/A:1011556926362.

[16] D.E. Merewether, Transient currents induced on a metallic body of revolution by an electromagnetic pulse, IEEE Transactions on Electromagnetic Compatibility EMC-13 (2) (1971) 41–44, doi:10.1109/TEMC.1971.303117.

[17] R. Holland, THREDE: A free-field EMP coupling and scattering code, IEEE Transactions on Nuclear Science 24 (6) (1977) 2416–2421, doi:10.1109/TNS.1977.4329229.

[18] H. Bériot, A. Modave, An automatic perfectly matched layer for acoustic finite element simulations in convex domains of general shape, International Journal for Numerical Methods in Engineering 122 (5) (2021) 1239–1261, doi:10.1002/nme.6560.

[19] A. Modave, J. Lambrechts, C. Geuzaine, Perfectly matched layers for convex truncated domains with discontinuous Galerkin time domain simulations, Computers and Mathematics with Applications 73 (4) (2017) 684–700, doi:10.1016/j.camwa.2016.12.027.

[20] J. Larsen, H. Dancy, Open boundaries in short wave simulations — A new approach, Coastal Engineering 7 (3) (1983) 285–297, doi:10.1016/0378-3839(83)90022-4.

[21] A. Rodrigues, Z. Dimitrovová, The Caughey Absorbing Layer Method – Implementation and validation in Ansys software, Latin American Journal of Solids and Structures 12 (8) (2015) 1540–1564, doi:10.1590/1679-78251713.
[22] X. Ma, Q. Feng, L. Liu, J. Xu, P. Zhang, H. Chen, A non-local method in peridynamic theory for simulating elastic wave propagation in solids, Applied Mathematical Modelling 103 (2022) 360–375, doi:10.1016/j.apm.2021.10.041.
[23] D. Komatitsch, J. Tromp, A perfectly matched layer absorbing boundary condition for the second-order seismic wave equation, Geophysical Journal International 154 (1) (2003) 146–153, doi:10.1046/j.1365-246X.2003.01950.x.
[24] A. Bermúdez, L. Hervella-Nieto, A. Prieto, R. Rodríguez, An optimal perfectly matched layer with unbounded absorbing function for time-harmonic acoustic scattering problems, Journal of Computational Physics 223 (2) (2007) 469–488, doi:10.1016/j.jcp.2006.09.018.
[25] D. Kim, A modified PML acoustic wave equation, Symmetry 11 (2) (2019) 1–15, doi:10.3390/sym11020177.
[26] P.G. Petropoulos, On the termination of the perfectly matched layer with local absorbing boundary conditions, Journal of Computational Physics 143 (2) (1998) 665–673, doi:10.1006/jcph.1998.5979.
[27] F. Collino, P.B. Monk, Optimizing the perfectly matched layer, Computer Methods in Applied Mechanics and Engineering 164 (1-2) (1998) 157–171, doi:10.1016/S0045-7825(98)00052-8.
[28] W.C. Chew, W.H. Weedon, A 3D perfectly matched medium from modified maxwell's equations with stretched coordinates, Microwave and Optical Technology Letters 7 (13) (1994) 599–604, doi:10.1002/mop.4650071304.
[29] W.C. Chew, Q.H. Liu, Perfectly matched layers for elastodynamics: a new absorbing boundary condition, Journal of Computational Acoustics 4 (4) (1996) 341–359, doi:10.1142/S0218396X96000118.
[30] B. Alpert, L. Greengard, T. Hagstrom, Nonreflecting boundary conditions for the time-dependent wave equation, Journal of Computational Physics 180 (1) (2002) 270–296, doi:10.1006/jcph.2002.7093.
[31] L. Xin, L. Yang, R. Zhi-Ming, C. Xiao-Hui, L. Bei, X. Shi-Gang, Z. Le-Kai, Hybrid absorbing boundary condition for three-dimensional elastic wave modeling, Applied Geophysics 14 (2) (2017) 270–278, doi:10.1007/s11770-017-0623-z.
[32] A. Oskooi, S.G. Johnson, Distinguishing correct from incorrect PML proposals and a corrected unsplit PML for anisotropic, dispersive media, Journal of Computational Physics 230 (7) (2011) 2369–2377, doi:10.1016/j.jcp.2011.01.006.
[33] J.G. Blaschak, G.A. Kriegsmann, A comparative study of absorbing boundary conditions, Journal of Computational Physics 77 (1) (1988) 109–139, doi:10.1016/0021-9991(88)90159-3.
[34] R. Clayton, B. Engquist, Absorbing boundary conditions for acoustic and elastic waves equations, Bulletin of the Seismological Society of America 67 (6) (1977) 1529–1540, doi:10.1785/BSSA0670061529.
[35] R.L. Higdon, Absorbing boundary conditions for difference approximations to the multi-dimensional wave equation, Mathematics of Computation 47 (176) (1986) 437–459, doi:10.2307/2008166.
[36] A. Modave, A. Atle, J. Chan, T. Warburton, A GPU-accelerated nodal discontinuous Galerkin method with high-order absorbing boundary conditions and corner/edge compatibility, International Journal for Numerical Methods in Engineering 112 (11) (2017) 1659–1686, doi:10.1002/nme.5576.
[37] V.A. Gordin, A.A. Shemendyuk, Discrete transparent boundary conditions for the equation of rod transverse vibrations, Applied Mathematical Modelling 88 (2020) 550–572, doi:10.1016/j.apm.2020.06.050.
[38] R.L. Higdon, Numerical absorbing boundary conditions for the wave equation, Mathematics of Computation 49 (179) (1987) 65–90, doi:10.2307/2008250.
[39] D. Givoli, B. Neta, I. Patlashenko, Finite element analysis of time-dependent semi-infinite wave-guides with high-order boundary treatment, International Journal for Numerical Methods in Engineering 58 (13) (2003) 1955–1983, doi:10.1002/nme.842.
[40] D. Givoli, B. Neta, High-order non-reflecting boundary conditions for dispersive waves, Wave Motion 37 (3) (2003) 257–271, doi:10.1016/S0165-2125(02)00074-4.
[41] T. Hagstrom, M.L. De Castro, D. Givoli, D. Tzemach, Local high-order absorbing boundary conditions for time-dependent waves in guides, Journal of Computational Acoustics 15 (1) (2007) 1–22, doi:10.1142/S0218396X07003184.
[42] V.J. van Joolen, B. Neta, D. Givoli, High-order Higdon-like boundary conditions for exterior transient wave problems, International Journal for Numerical Methods in Engineering 63 (7) (2005) 1041–1068, doi:10.1002/nme.1322.
[43] J.A. Pereda, A. Serroukh, A. Grande, A. Vegas, Implementation of absorbing boundary conditions based on the second-order one-way wave equation in the LOD- and the ADI-FDTD methods, IEEE Antennas and Wireless Propagation Letters 11 (2) (2012) 981–983, doi:10.1109/LAWP.2012.2212411.
[44] D. Baffet, D. Givoli, On the stability of the high-order Higdon Absorbing Boundary Conditions, Applied Numerical Mathematics 61 (6) (2011) 768–784, doi:10.1016/j.apnum.2011.01.010.
[45] T. Matsuno, False reflection of waves at the boundary due to the use of finite differences, Journal of the Meteorological Society of Japan. Ser. II 44 (2) (1966) 145–157, doi:10.2151/jmsj1965.44.2_145.
[46] F. Collino, C. Tsogka, Application of the perfectly matched absorbing layer model to the linear elastodynamic problem in anisotropic heterogeneous media, Geophysics 66 (1) (2001) 294–307, doi:10.1190/1.1444908.
[47] R. Shi, S. Wang, J. Zhao, An unsplit complex-frequency-shifted PML based on matched Z-transform for FDTD modelling of seismic wave equations, Journal of Geophysics and Engineering 9 (2) (2012) 218–229, doi:10.1088/1742-2132/9/2/218.
[48] S. Abarbanel, D. Gottlieb, On the construction and analysis of absorbing layers in CEM, Applied Numerical Mathematics 27 (4) (1998) 331–340, doi:10.1016/S0168-9274(98)00018-X.
[49] M. Kuzuoglu, R. Mittra, Frequency dependence of the constitutive parameters of causal perfectly matched anisotropic absorbers, IEEE Microwave and Guided Wave Letters 6 (12) (1996) 447–449, doi:10.1109/75.544545.
[50] A. Bermúdez, O. Crego, A. Prieto, Upwind finite element-PML approximation of a novel linear potential model for free surface flows produced by a floating rigid body, Applied Mathematical Modelling 103 (2022) 824–853, doi:10.1016/j.apm.2021.11.004.
[51] Y. Shen, V. Giurgiutiu, Effective non-reflective boundary for Lamb waves: Theory, finite element implementation, and applications, Wave Motion 58 (2015) 22–41, doi:10.1016/j.wavemoti.2015.05.009.
[52] S.K. Kar, R.P. Turco, Formulation of a lateral sponge layer for limited-area shallow-water models and an extension for the vertically stratified case, Monthly Weather Review 123 (5) (1995) 1542–1559, doi:10.1175/1520-0493(1995)123<1542:FOALSL>2.0.CO;2.
[53] F.Q. Hu, On absorbing boundary conditions for linearized Euler equations by a perfectly matched layer, Journal of Computational Physics 129 (1) (1996) 201–219, doi:10.1006/jcph.1996.0244.
[54] A. Taflove, Advances in Computational Electrodynamics: The Finite-Difference Time-Domain Method, 1st, Artech House, Boston, MA, 1998.
[55] J.A. Roden, S.D. Gedney, Convolution PML (CPML): An efficient FDTD implementation of the CFS-PML for arbitrary media, Microwave and Optical Technology Letters 27 (5) (2000) 334–339, doi:10.1002/1098-2760(20001205)27:5<334::AID-MOP14>3.0.CO;2-A.
[56] M.A. Dablain, The application of high-order differencing to the scalar wave equation, Geophysics 51 (1) (1986) 54–66, doi:10.1190/1.1442040.
[57] R. Kosloff, D. Kosloff, Absorbing boundaries for wave propagation problems, Journal of Computational Physics 376 (2) (1986) 363–376, doi:10.1016/0021-9991(86)90199-3.
[58] Q.-H. Liu, J. Tao, The perfectly matched layer for acoustic waves in absorptive media, The Journal of the Acoustical Society of America 102 (4) (1997) 2072–2082, doi:10.1121/1.419657.
[59] D. Pasalic, R. McGarry, Convolutional Perfectly Matched Layer for isotropic and anisotropic acoustic wave equations, in: SEG Technical Program Expanded Abstracts 2010, Society of Exploration Geophysicists, 2010, pp. 2925–2929, doi:10.1190/1.3513453.
[60] Q.H. Liu, Perfectly matched layers for elastic waves in cylindrical and spherical coordinates, Journal of the Acoustical Society of America 105 (4) (1999) 2075–2084, doi:10.1121/1.426812.
[61] C. Peng, M. Nafi Toksöz, An optimal absorbing boundary condition for elastic wave modeling, Geophysics 60 (1) (1995) 296–301, doi:10.1190/1.1443758.

[62] M. Israeli, S.A. Orszag, Approximation of radiation boundary conditions, Journal of Computational Physics 41 (1) (1981) 115–135, doi:10.1016/0021-9991(81)90082-6.
[63] Y. Liu, M.K. Sen, A hybrid scheme for absorbing edge reflections in numerical modeling of wave propagation, Geophysics 75 (2) (2010) A1–A6, doi:10.1190/1.3295447.
[64] Y. Liu, M.K. Sen, An improved hybrid absorbing boundary condition for wave equation modeling, Journal of Geophysics and Engineering 15 (6) (2018) 2602–2613, doi:10.1088/1742-2140/aadd31.
[65] G. Xu, A.M. Hamouda, B.C. Khoo, Time-domain simulation of second-order irregular wave diffraction based on a hybrid water wave radiation condition, Applied Mathematical Modelling 40 (7-8) (2016) 4451–4467, doi:10.1016/j.apm.2015.11.034.
[66] A. Logg, K.-A. Mardal, G.N. Wells, Automated Solution of Differential Equations by the Finite Element Method, 1st, Springer-Verlag Berlin Heidelberg, New York, 2012, doi:10.1007/978-3-642-23099-8.
[67] E. Mesquita, R. Pavanello, Numerical methods for the dynamics of unbounded domains, Computational and Applied Mathematics 24 (1) (2005) 1–26, doi:10.1590/S0101-82052005000100001.
[68] M. Gardner, Mathematical Carnival, 5st, The Mathematical Association of America, Washington, D.C., 1989.
[69] K.F. Graff, Wave Motion in Elastic Solids, 1st ed., Dover Publications, New York, NY, 1975.
[70] H. Georgi, The Physics of Waves, 1st, Prentice Hall, Englewood Cliffs, N. J., 1993.
[71] D. Royer, E. Dieulesaint, Elastic Waves in Solids I: Free and Guided Propagation, 1st ed., Springer-Verlag, Berlin, 2000.
[72] I.G. Main, Vibrations and Waves in Physics, 3rd, Cambridge University Press, Cambridge, 1993, doi:10.1017/CBO9781139170567.
[73] J.E. Laier, Finite element solution of wave equation with reduction of the velocity dispersion and spurious reflection, Latin American Journal of Solids and Structures 17 (8) (2020) 1–10, doi:10.1590/1679-78256221.
[74] J.D. Romano, R.H. Price, A simple graphical method for calculating the standing wave frequencies on a rectangular membrane, American Journal of Physics 88 (8) (2020) 605–611, doi:10.1119/10.0001299.
[75] J.A. Sethian, A. Vladimirsky, Fast methods for the Eikonal and related Hamilton-Jacobi equations on unstructured meshes, Proceedings of the National Academy of Sciences 97 (11) (2000) 5699–5703, doi:10.1073/pnas.090060097.
[76] P.G. Tucker, C.L. Rumsey, P.R. Spalart, R.B. Bartels, R.T. Biedron, Computations of Wall Distances Based on Differential Equations, AIAA Journal 43 (3) (2005) 539–549, doi:10.2514/1.8626.
[77] L.F. Sá, P.V. Yamabe, B.C. Souza, E.C. Silva, Topology optimization of turbulent rotating flows using Spalart–Allmaras model, Computer Methods in Applied Mechanics and Engineering 373 (2021) 113551, doi:10.1016/j.cma.2020.113551.
[78] J. Gutiérrez-Vega, S. Chávez-Cerda, R. Rodríguez-Dagnino, Free oscillations in an elliptic membrane, Revista Mexicana de Fisica 45 (6) (1999) 613–622.
[79] T.E. Oliphant, Python for Scientific Computing, Computing in Science & Engineering 9 (3) (2007) 10–20, doi:10.1109/MCSE.2007.58.
[80] Y. Wang, Frequencies of the ricker wavelet, Geophysics 80 (2) (2015) A31–A37, doi:10.1190/geo2014-0441.1.
[81] J.M. Carcione, G.C. Herman, A.P.E. ten Kroode, Y2K Review Article: Seismic modeling, Geophysics 67 (4) (2002) 1304–1325, doi:10.1190/1.1500393.
[82] G.S. Martin, R. Wiley, K.J. Marfurt, Marmousi2: An elastic upgrade for Marmousi, Thee Leading Edge 25 (2) (2006) 156–166, doi:10.1190/1.2172306.
[83] J.C. Gutiérrez-Vega, R.M. Rodríguez-Dagnino, M.A. Meneses-Nava, S. Chávez-Cerda, Mathieu functions, a visual approach, American Journal of Physics 71 (3) (2003) 233–242, doi:10.1119/1.1522698.
[84] S.L. Garret, Understanding Acoustics: An Experimentalist's View of Sound and Vibration, 2nd ed., ASA Press/Springer, 2020, doi:10.1007/978-3-030-44787-8.
[85] D.E. Knuth, The METAFONTbook, 160th, Addison-Wesley Publishing Company, Reading, MA, 1986.
[86] D. Salomon, Computer Graphics and Geometric Modeling, 1st, Springer Science+Business Media, LLC, New York, NY, 1999.
[87] F. Jacobsen, P.M. Juhl, Fundamentals of General Linear Acoustics, 1st ed., John Wiley & Sons Ltd, Chichester, West Sussex, UK, 2013.
[88] J.S. Arora, Introduction to Optimum Design, 2nd ed., Elsevier Academic Press, San Diego, CA, 2004.
[89] G.B. Thomas, R.L. Finney, Calculus and Analytic Geometry, 9th ed, Addison-Wesley Publishing Company, Inc., New York, 1996.
[90] D.G. Zill, First Course in Differential Equations with Modeling Applications, 6th, Cengage Learning, Pacific Grove, CA, 1996.
[91] M. Abramowitz, I.A. Stegun, Handbook of Mathematical Functions: with Formulas, Graphs, and Mathematical Tables, 9th, Dover Publications, New York, 1970.
[92] H.G. Pulido, R.d.l.V. Salazar, Análisis y Diseño de Experimentos, 2nd, McGraw-Hill Interamericana Editores S.A. de C.V., Mexico, D. F., 2008.